Petroleum Science 23 (2026) 7374–7398

Contents lists available at ScienceDirect

Petroleum Science

journal homepage: www.keaipublishing.com/en/journals/petroleum-science

Original Paper

Unlocking synergistic effects in chemical-assisted CO_2 flooding: Multiscale optimization of chemicals for enhanced oil recovery and carbon utilization

Quan-Ling Qin [a,c], Jian Hou [a,c,*], Kang Zhou [b,**], Jia-Rui Zhang [a,c], Hao-Yu Zheng [a,c], Yong-Sheng Liu [a,c], Bei Wei [a,c], Teng Lu [a,c], Yong-Ge Liu [a,c], Wei-Bing Tian [a,c], Qing-Jun Du [a,c]

[a] State Key Laboratory of Deep Oil and Gas, China University of Petroleum (East China), Qingdao, 266580, Shandong, China
[b] College of Energy and Mining Engineering, Shandong University of Science and Technology, Qingdao, 266590, Shandong, China
[c] School of Petroleum Engineering, China University of Petroleum (East China), Qingdao, 266580, Shandong, China

ARTICLE INFO

Article history:
Received 5 February 2026
Received in revised form
9 May 2026
Accepted 28 June 2026
Available online 6 July 2026

Edited by Meng-Jiao Zhou

Keywords:
Chemical-assisted CO_2 flooding
Multiscale simulation
Concentration optimization
Microscopic mechanism
Enhanced oil recovery (EOR)

ABSTRACT

Improving CO_2 flooding in deep oil reservoirs requires a mechanistic understanding of how chemical additives regulate oil-CO_2 interactions across scales. In this study, theoretical calculations, molecular dynamics (MD), and computational fluid dynamics (CFD) were integrated to investigate the microscopic mechanisms and concentration-optimization strategy of chemical-assisted CO_2 flooding. A multiscale model was established to account for the effects of chemicals on CO_2 dissolution, extraction, and diffusion in oil, thereby linking molecular interactions with microscopic seepage behavior. The main results are as follows: (1) a newly defined miscibility-degree index showed that Span-series surfactants, particularly 0.5 wt% Span 20, significantly enhanced CO_2-oil miscibility; (2) the effects of chemicals on CO_2 mass transfer were concentration dependent, with 0.1 wt% Span 20 increasing CO_2 solubility in oil by 20.64% and the diffusion coefficient by 12.38%, whereas extraction efficiency increased by 44.60% at 0.5 wt%; (3) chemicals improved oil recovery through coupled mechanisms, including reduced oil-wall interaction energy (with the optimum effect at 0.1 wt% Span 20) and strengthened molecular interactions between CO_2 and oil; (4) pore type influenced recovery efficiency, with Span-series chemicals markedly improving recovery from small and blind-end pores, whereas anionic surfactant sodium bis(2-ethylhexyl) sulfosuccinate (AOT) mainly enhanced recovery from small pores; and (5) 0.2 wt% Span 20 was identified as the optimal concentration, while adsorption loss requires the practical injection concentration to be adjusted to 0.54%–0.68%. These findings provide a theoretical basis and methodological support for designing chemical-assisted CO_2 flooding schemes for deep reservoirs.
© 2026 The Authors. Publishing services by Elsevier B.V. on behalf of KeAi Communications Co. Ltd. This is an open access article under the CC BY license (http://creativecommons.org/licenses/by/4.0/).

1. Introduction

With the growing scarcity of global petroleum resources and the progressive depletion of conventional oil and gas reserves, improving the recovery efficiency of challenging reservoirs has become increasingly imperative. The development of deep oil reservoirs has emerged as a critical focus for the petroleum industry, where water flooding and gas flooding serve as primary methods to enhance crude oil recovery (Xiong et al., 2021; Zhang et al., 2022a, 2024). Among various gas injection techniques, CO_2 flooding has proven to be an effective enhanced oil recovery (EOR) method with broad application prospects in deep reservoirs, particularly under the dual-carbon goals (Alharthy et al., 2017; Xiang et al., 2023; Song et al., 2023). Studies have shown that injected CO_2 enhances oil recovery primarily through dissolution, diffusion, and miscibility mechanisms, which result in crude oil swelling and viscosity reduction (Kumar et al., 2022; Li et al., 2022a; Guo et al., 2022; Feng et al., 2024). For low-permeability reservoirs characterized by deep burial, strong heterogeneity,

* Corresponding author.
** Corresponding author.
E-mail addresses: sllx_upc@126.com (J. Hou), zhoukang_upc@163.com (K. Zhou).
Peer review under the responsibility of China University of Petroleum (Beijing).

https://doi.org/10.1016/j.petsci.2026.06.050
1995-8226/© 2026 The Authors. Publishing services by Elsevier B.V. on behalf of KeAi Communications Co. Ltd. This is an open access article under the CC BY license (http://creativecommons.org/licenses/by/4.0/).

and high minimum miscibility pressure (MMP), researchers have proposed a high-pressure miscible CO_2 flooding and storage model. This approach achieves miscibility with heavy hydrocarbon crude oils through continuous bidirectional mass transfer between phases, thereby substantially improving both oil displacement efficiency and CO_2 storage capacity (Yang, 2020; Yang et al., 2024). Previous studies confirm that CO_2-EOR is mainly driven by intense interactions between CO_2 and crude oil, including dissolution, extraction, and diffusion. To further optimize CO_2 flooding performance, various strategies have been investigated, such as adjusting injection rates, modifying temperatures, and incorporating chemical additives to enhance CO_2-crude oil mass transfer (Jiang et al., 2024). Chemical agents, including methanol, acetone, surfactants, and propanol, have been shown to significantly reduce the interfacial tension between CO_2 and crude oil as well as the MMP, thereby promoting miscibility and improving oil recovery (Zhang et al., 2018; Liu et al., 2022a; Wang et al., 2023; Song et al., 2024; Türkmenoğlu and Önel, 2025). Although alcohols can reduce MMP by 9.21%, ethers and ketones (e.g., petroleum ether and acetone) exhibit superior performance under high-temperature and high-pressure conditions (Song et al., 2024). As a cosolvent, dimethyl ether markedly increases CO_2 solubility and the swelling coefficient of crude oil while reducing interfacial free energy and tension, achieving a 43% MMP reduction for light crude oils (Xie et al., 2025). Experimental studies have also demonstrated that addition of ethylene glycol butyl ether and Span 80 significantly enhances CO_2-crude oil interactions and recovery (Li et al., 2023a). Additionally, aerogel nanoparticles provide a novel route to improve CCUS efficiency by adsorbing asphaltene molecules and mitigating reservoir plugging (Lu et al., 2024a). Consequently, exploiting the synergistic effects of chemical agents and CO_2 flooding offers a promising pathway for optimizing displacement efficiency in deep oil reservoirs.

Recent experimental studies on CO_2 flooding in deep oil reservoirs have made significant advances, preliminarily elucidating the interaction mechanisms between CO_2 and crude oil under high-temperature and high-pressure (HPHT) conditions (Lei et al., 2022; Zhang et al., 2023; Pan et al., 2024). Research has demonstrated the CO_2 selective extraction capability toward different crude oil components. While short-chain hydrocarbons (e.g., light components) exhibit relatively weak interactions with CO_2, rendering light oil more readily extractable, the extraction capacity of CO_2 for heavy oil is substantially enhanced under deep-reservoir HPHT conditions (Li et al., 2021; Chowdhury et al., 2022). When supercritical CO_2 directly contacts crude oil, it recovers micro-residual oil primarily by extracting light and intermediate components. Alternatively, contact between CO_2 and water generates carbonated water, which recovers residual oil through dissolution and swelling. However, asphaltene deposition becomes pronounced after injection, particularly in low-permeability zones (Zhang et al., 2022b). In deep reservoirs, higher pressures promote the initiation of extraction and miscibility processes. The CO_2-oil phase behavior manifests as swelling, immiscible extraction, and miscible extraction, all of which are governed by dissolution, capillary effects, and vaporization mechanisms (Zhang et al., 2023). In addition to fluid-fluid interactions, pore conditions significantly influence flooding efficiency through pore-scale effects and structural characteristics. CO_2 diffusion, adsorption, and miscibility in nanoporous media are strongly affected by pore wettability. Experimental results indicate that CO_2 preferentially diffuses into the oil phases in CO_2-wet regions, and the MMP decreases as pore size decreases, suggesting enhanced miscibility in smaller pores (Wang et al., 2022, 2024a; Sun et al., 2024). Pore tortuosity markedly suppresses CO_2 diffusion in crude oil (Gao et al., 2019), while adsorbed layers on pore walls can shift fluid flow from slip to negative slip, thereby reducing CO_2 permeability (Yuan et al., 2023). Furthermore, the migration of CO_2 within the reservoir during CO_2 flooding is constrained by multiple factors, including the staged characteristics of multiscale transport, fluid occurrence patterns dominated by heterogeneous pore-throat structures, and the startup pressure-gradient effects and flow-regime transitions induced by strong fluid-solid coupling (Chen et al., 2022; Liu et al., 2025a, 2025b). These factors further increase the complexity of regulating fluid migration in deep oil reservoirs.

Molecular and pore-scale simulations have become essential tools for investigating CO_2 flooding mechanisms. Molecular simulations provide detailed insights into nanoscale interactions within CO_2-oil-rock systems, including miscibility, adsorption, diffusion, and interfacial alterations (Luo et al., 2023; Xue et al., 2023; Cui et al., 2023; Lu et al., 2024b). Studies have shown that CO_2 enhances oil recovery through three primary mechanisms: (1) reduction of interfacial tension and crude oil viscosity, which improve oil mobility (Li et al., 2024); (2) competitive adsorption and dissolution that strip crude oil from rock surfaces (Lu et al., 2022); (3) selective extraction that preferentially recovers saturates over aromatics (Lu et al., 2022). However, certain limitations remain. For instance, the thickness of the adsorbed oil layer tends to increase during depressurization, thereby reducing effective pore volume and impeding fluid flow (Huang et al., 2024; Wang et al., 2025). In addition, enhanced organic content in nanopores weakens the interactions between light hydrocarbon and pore walls but promotes the adsorption of heavy hydrocarbon, which hinders oil production (Hu et al., 2025). Pore structure plays a critical role in CO_2 flooding efficiency. Oil recovery correlates strongly with pore size: in small pores, high-pressure CO_2 injection effectively recovers heavy components, whereas in large pores, comparable recovery can be achieved even at lower pressures (Jin and Firoozabadi, 2016). Notably, CO_2 exhibits superior performance in smaller pores and with heavier hydrocarbon components. Mineral composition also influences recovery efficiency, with illite pores yielding the highest recovery, followed by quartz pores, while kerogen pores show the lowest recovery (Wang et al., 2024b). Extraction efficiency further varies by pore type: organic pores favor the recovery of C3 components, whereas inorganic pores enhance the extraction of C1 and C2 (Zhang et al., 2020a).

In pore-scale modeling, the phase-field method has been widely employed to simulate immiscible CO_2 flooding by tracking phase-interface evolution, enabling systematic investigation of the effects of capillary number, viscosity ratio, gravity, wettability, density, and interfacial tension (Zhu et al., 2017; Song et al., 2022). For miscible flooding, coupled Navier-Stokes and convection-diffusion equations are commonly used to characterize fluid flow and component transport (Afshari et al., 2018; Li et al., 2023b; Yan et al., 2023). Simulations reveal distinct displacement patterns: miscible flooding initially exhibits piston-like displacement that gradually transitions to viscous fingering, with oil being sequentially produced from large, medium, and small pores. In contrast, immiscible flooding sustains viscous fingering that intensifies after breakthrough, with oil primarily produced from large pores (Ren et al., 2024). Further analysis confirms three key recovery mechanisms in miscible flooding: viscosity reduction (which affects production rate), desorption (which determines ultimate recovery), and extraction (which is critical in blind-end pores) (Zhu et al., 2024).

Although traditional experiments provide reliable evidence, they are often expensive, time-consuming, and limited in their ability to resolve microscopic fluid interactions. Computational simulations provide a complementary and efficient approach for

revealing mechanisms from the molecular to pore scales. Multiscale simulation has therefore attracted increasing attention. By integrating molecular simulations with CFD, oil displacement processes can be understood and optimized more comprehensively. However, few studies have examined chemical-assisted CO_2 flooding in deep reservoirs using a multiscale framework, particularly for chemical screening and concentration optimization. Here, we develop a molecular-to-pore-scale modeling framework to investigate the synergistic mechanisms of chemical-assisted CO_2 flooding in deep reservoirs. The optimal chemicals and concentrations are then identified to support efficient deep-reservoir development. The results provide theoretical guidance for optimizing chemical-assisted CO_2 flooding schemes and improving oil recovery. This study also demonstrates the value of multiscale simulation as a methodological reference for future work on chemically assisted CO_2 flooding.

2. Methodology

The overall workflow of this study is shown in Fig. 1. First, theoretical calculations were used to determine fluid viscosity and density, which provided the physical-property inputs for the subsequent CFD simulations. Molecular simulations were then performed to evaluate the effects of chemical agents on CO_2 extraction, diffusion, and dissolution in oil, yielding chemically regulated parameters for the CFD model. CFD simulations were subsequently used to resolve microscopic flow behavior and optimize the operational scheme. Finally, the simulation results were validated through microscopic seepage experiments. Within this multiscale coupling framework, cross-scale parameter transfer followed a defined logic. The diffusion coefficients of components affected by chemical agents were calculated from molecular dynamics simulations using Einstein's equation and then introduced into the pore-scale convection-diffusion equation. In addition, molecular-scale interaction energies were used to quantify how chemical agents regulate CO_2 dissolution and extraction. In the CFD model, this regulatory mechanism was represented by incorporating a reaction source term into the convection-diffusion equation, thereby mapping molecular-level chemical effects onto macroscopic mass transfer.

2.1. Theoretical calculation

To construct a molecular model that represents reservoir conditions accurately, the Peng-Robinson equation of state (PR-EOS) was used to calculate the densities of hydrocarbon molecules and CO_2 at different temperatures and pressures (Peng and Robinson, 1976). The PR-EOS is well suited to petroleum reservoir engineering because it combines moderate computational cost with reliable physical-property prediction. This widely used cubic equation of state also predicts the phase behavior of hydrocarbon components and mixtures under HPHT conditions with good accuracy. By accounting for intermolecular attractive and repulsive forces, the PR-EOS describes the non-ideal behavior of deep-reservoir fluids. The general expression of the PR-EOS is:

$$P = \frac{RT}{V-b} - \frac{a}{V(V+b)+b(V-b)} \tag{1}$$

$$a = 0.45724\frac{R^2T_c^2}{P_c}\left(1+m\left(1-\sqrt{\frac{T}{T_c}}\right)\right)^2 \tag{2}$$

$$m = 0.37464 + 1.54226\omega - 0.26992\omega^2 \tag{3}$$

$$b = \frac{0.07780RT_c}{P_c} \tag{4}$$

The above equation can be rewritten in the cubic form of the compressibility factor:

$$Z^3 - (1-B)Z^2 + \left(A - 2B - 3B^2\right)Z - \left(AB - B^2 - B^3\right) = 0 \tag{5}$$

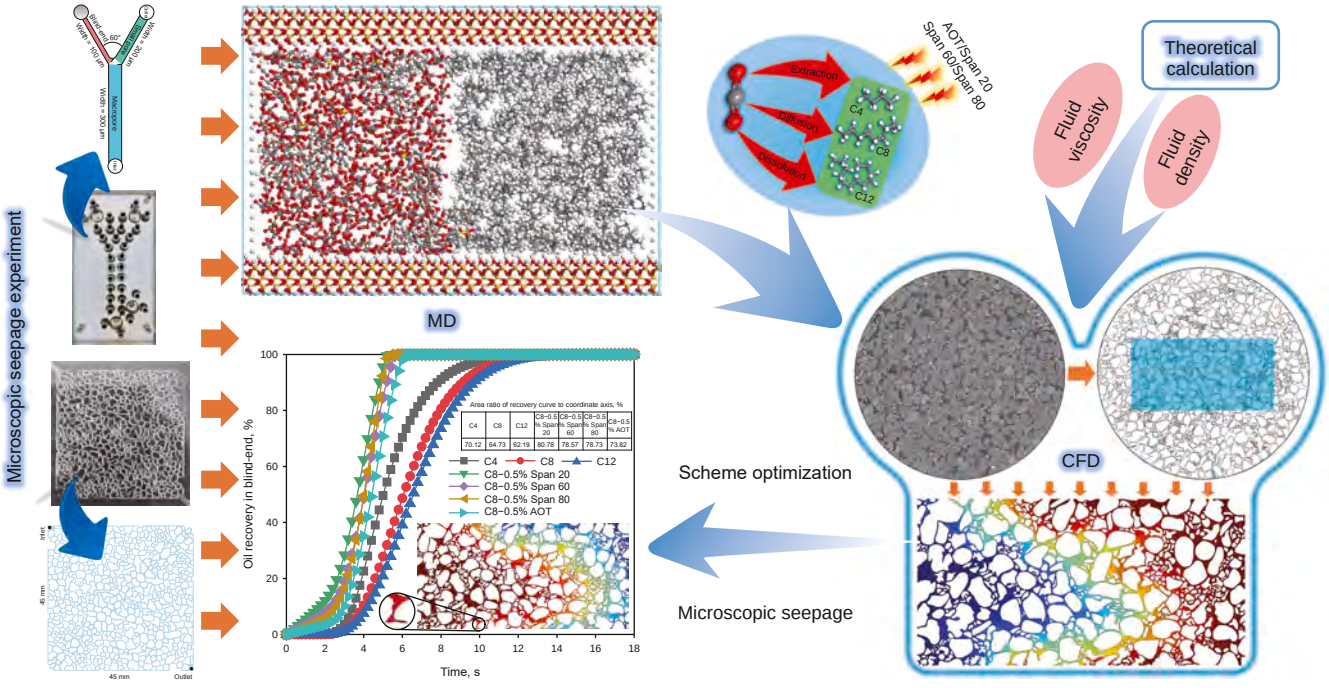


Fig. 1. Flowchart of the research methodology.

$$A = \frac{aP}{R^2T^2} \tag{6}$$

$$B = \frac{bP}{RT} \tag{7}$$

The density of hydrocarbon and CO_2 molecules is calculated using the following formula:

$$\rho = \frac{PM}{ZRT} \tag{8}$$

where P is the pressure, Pa; T is the temperature, K; P_c is the critical pressure, Pa; T_c is the critical temperature, K; ω is the acentric factor; Z is the compressibility factor; M is the molar mass of the molecule, kg/mol; R is the ideal gas constant, 8.314 J·mol^{-1}·K^{-1}; and ρ is the density of the molecule, kg/m^3.

The viscosity of CO_2 was calculated using the model proposed by Heidaryan et al. (2011), and the viscosities of alkanes were determined using the model developed by Pedersen et al. (1984). These parameters provided the input conditions for subsequent CFD simulations and ensured that the model represented the physical properties of CO_2 and oil under deep-reservoir conditions.

2.2. Molecular simulation

Molecular simulation has become a critical methodology for investigating molecular motion and interaction mechanisms. In molecular simulation systems, intermolecular interactions are typically described using force field parameters. Among these, the COMPASS force field is one of the most widely adopted due to its versatility and high accuracy. This force field incorporates comprehensive parameter sets for both organic and inorganic materials, enabling precise simulations of a range of substances, including small organic molecules, inorganics, polymers, metal ions, metal oxides, and metallic materials (Sun, 1998; Yang et al., 2021). In studies of CO_2 flooding, the COMPASS force field has proven effective in accurately characterizing interactions between CO_2 molecules and hydrocarbon molecules. It offers particular advantages in simulating key processes such as interfacial adsorption and molecular diffusion (Li et al., 2021). Overall, molecular simulations provide valuable insights into the microscopic interaction mechanisms within CO_2-oil-rock systems under HPHT conditions, offering molecular-level theoretical support for understanding displacement processes.

2.2.1. Construction of the molecular model

In this study, Span-series surfactants and anionic surfactant sodium bis(2-ethylhexyl) sulfosuccinate (AOT) were selected as the target chemical agents, primarily due to their excellent thermal and chemical stability (Lu et al., 2023). Compared with polymers that are prone to thermal degradation at high temperatures or alkaline solutions that tend to precipitate in high-salinity formation water, the non-ionic surfactant Span 20 maintains high interfacial activity under elevated temperatures (Moniruzzaman et al., 2010). In addition, the unique double-branched hydrophobic tail structure of AOT, combined with the strong affinity of Span-series surfactants for CO_2, endows them with excellent solubility in supercritical CO_2. This enables significant reduction of the MMP between CO_2 and crude oil (Wang et al., 2023; Zhang et al., 2020b). More importantly, these small-molecule chemical agents can readily penetrate pore spaces that are inaccessible to polymers (Li et al., 2023a), effectively inhibiting the deposition and adhesion of polar components from crude oil on pore walls, thereby ensuring long-term effectiveness of fluid regulation in deep reservoirs (Zhang et al., 2018).

First, molecular models of CO_2, C4, C8, C12, AOT, Span 20, Span 60, Span 80, and the pore walls were constructed based on their molecular formulas (Fig. 2(a)). The pore walls were modeled using hydroxylated silica (SiO_2-H) arranged in an ordered configuration to form fixed top and bottom boundaries of the simulation box. The dimensions of the simulation box were 78.61 Å × 34.04 Å × 54.07 Å, with a 42 Å vacuum layer placed between the walls to accommodate the fluid molecules (Fig. 2(b)). Oil, CO_2, and chemical agents were then positioned on opposite sides of the pore within the simulation box to establish the initial CO_2-oil-chemical agent system. Fig. 2(b) shows the construction of the simulation box for the CO_2-C8 system; the same methodology was applied for to the other systems.

2.2.2. Molecular dynamics simulations

Prior to the molecular dynamics simulations, all molecular structures were subjected to geometry optimization to achieve their global minimum-energy configurations. This step eliminates high-energy conformations arising from molecular overlap or unreasonable spatial arrangements during model construction, thereby ensuring that the molecules reside in their most stable energy states. It also helps prevent simulation instability and convergence issues caused by excessively high initial energies (Guénolé et al., 2020). During the simulations, the Nose-Hoover thermostat and Berendsen barostat were employed to precisely control temperature and pressure, maintaining the system at 388.15 K and 55 MPa to replicate actual supercritical CO_2 flooding conditions (Li et al., 2022b). The molecular dynamics simulations were run for 1000 ps with a timestep of 1 fs, and trajectory data were recorded every 1000 steps. This approach allowed

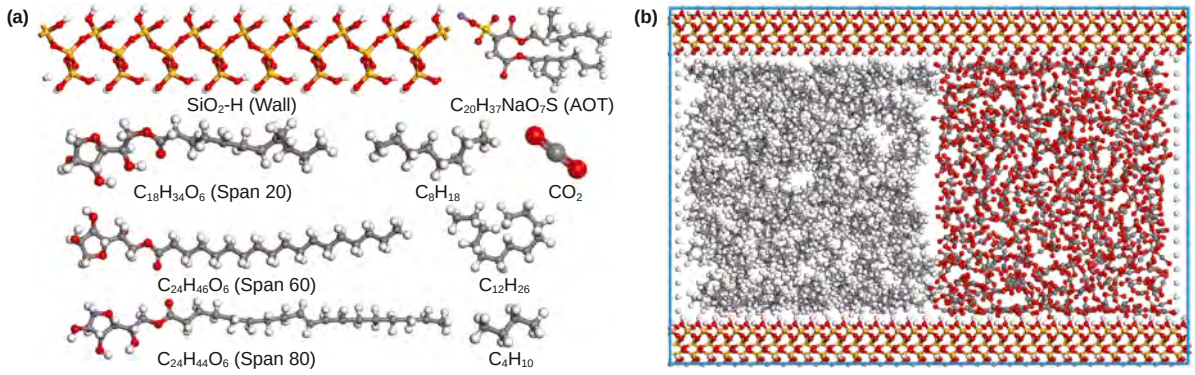


Fig. 2. Molecular models used in the simulations. **(a)** Molecular formulas and corresponding three-dimensional structures; **(b)** simulation box constructed for different molecule systems.

comprehensive capture of molecular distributions, interfacial behavior, and mass transfer characteristics throughout the system evolution, providing essential data for subsequent microscopic mechanism analysis.

2.2.3. Simulation analysis

In molecular simulations, the relationship between mean square displacement (MSD) and the diffusion coefficient provides a fundamental theoretical basis for analyzing particle diffusion behavior. By monitoring the temporal evolution of MSD, the diffusion coefficients of CO_2 molecules in different hydrocarbon systems can be accurately determined (Wang et al., 2024c). According to Einstein's diffusion theory, for freely diffusing particles, the MSD exhibits a linear relationship with time. The diffusion coefficient (D) is calculated as one-sixth of the slope of the MSD curve:

$$\mathrm{MSD} = \frac{1}{N}\sum_{i=1}^{N}[r_i(t) - r_i(0)]^2 \tag{9}$$

$$D = \frac{1}{6N}\lim_{t\to\infty}\frac{\mathrm{d}}{\mathrm{d}t}\sum_{i=1}^{N}[r_i(t) - r_i(0)]^2 = \frac{1}{6}K_{\mathrm{MSD}} \tag{10}$$

where N is the total number of diffusing molecules, $r_i(t)$ and $r_i(0)$ are the position vectors of molecule i at time t and 0, respectively, Å; K_{MSD} represents the slope of the MSD curve, and D is the diffusion coefficient, 10^{-8} m^2/s.

The intermolecular interaction energy quantifies the energetic contributions from various intermolecular forces, providing critical insights for into molecular behavior and interactions (Yu et al., 2023). A negative value of interaction energy indicates attractive forces, whereas a positive value indicates repulsive forces. The interaction energy is calculated as:

$$E_{\mathrm{A/B}} = E_{\mathrm{A+B}} - E_{\mathrm{A}} - E_{\mathrm{B}} \tag{11}$$

where $E_{\mathrm{A/B}}$ is the interaction energy between substance A and substance B in the system, kJ/mol; $E_{\mathrm{A+B}}$ is the total energy of the combined A–B system, kJ/mol; E_{A} is the total energy of substance A, kJ/mol; and E_{B} is the total energy of substance B, kJ/mol.

2.3. CFD simulation

2.3.1. Governing equations

CFD simulations are based on the Navier-Stokes equations and species transport equations to model fluid dynamics and mass transfer processes. The Navier-Stokes equations describe the motion of fluid, while the species transport equations govern the transport of different chemical species within the fluid. These equations are solved simultaneously using the finite element method for discretization, enabling accurate representation of complex flow and transport phenomena.

The Navier-Stokes equations, together with the continuity equation, characterize the dynamics of fluid motion and mass conservation (Aziz et al., 2020):

$$\rho\frac{\partial u}{\partial t} + \rho(u\cdot\nabla)u = \nabla\cdot\left[-pI + \mu\left(\nabla u + (\nabla u)^{\mathrm{T}}\right)\right] + F \tag{12}$$

$$\rho\nabla\cdot u = 0 \tag{13}$$

where ρ is the fluid density, kg/m^3; u is the fluid velocity, m/s; p is the fluid pressure, Pa; I is the unit tensor; μ is the dynamic viscosity, Pa·s; and F is the body force, N/m^3.

The miscible behavior of the fluid is characterized by the convection-diffusion equation. The Navier-Stokes equations are coupled with the mass transfer equation through the fluid velocity u. This coupling allows simultaneous description of the miscibility process and the displacement process between CO_2 and oil (Yan et al., 2023):

$$c_i(\nabla\cdot u) - \nabla\cdot(D_i\nabla c_i) + \left(\frac{\partial c_i}{\partial t} + u\cdot\nabla c_i\right) = R_i \tag{14}$$

$$\rho u = n\cdot\sum_i(\rho\cdot D_i\nabla c_i + \rho u c_i n) \tag{15}$$

where c_i represents the mass concentration of component; u is the fluid velocity, m/s; D_i is the diffusion coefficient of the component i, m^2/s; R_i denotes the mass source term due to reaction; n is the unit vector; and ρ is the fluid density, kg/m^3.

2.3.2. Porous media model

The pore structure model was first reconstructed from CT-scanned core slices by distinguishing pores from rock grains. The core images were processed through binarization to extract a realistic pore structure model while preserving key geological details to ensure structural authenticity. A rectangular porous medium domain, 3000 μm in length and 1500 μm in width, was then extracted from the center of the binarized image for pore-scale simulations. In addition, a 1500 μm × 200 μm rectangular injection zone was attached to the left side of the porous medium to facilitate fluid injection (Fig. 3).

The model was discretized using a free triangular mesh, generating a total of 351,377 elements. The mesh featured non-uniform element sizes, with minimum and maximum dimensions of 1.50 μm and 52.5 μm, respectively, which provided sufficient resolution for the complex pore geometries. Simulations were conducted under isothermal-isobaric conditions at 388.15 K and 55 MPa. No-slip boundary conditions were applied to all walls except the inlet and outlet. Initially, the porous medium was fully saturated with oil, while the left injection zone was pre-filled with CO_2 and the chemical agent. During dynamic simulation, CO_2 and chemical agent were co-injected at a constant velocity of 1×10^{-4} m/s through the left boundary (injection inlet), while the right boundary served as the pressure outlet maintained at 55 MPa to ensure miscible displacement throughout the process.

2.4. Microscopic seepage experiment

Ten micromodel experiments were conducted to validate the numerical model. The first five experiments utilized single-pore chips to isolate the effect of pore type (macropore, small pores, blind-end), while the remaining five employed etched-glass porous media chips to evaluate the performance of chemical additives during CO_2-oil-water displacement.

2.4.1. Materials

The fluids used included CO_2 (99.9%, Qingdao Deyi), deionized water (Wahaha Group), n-octane (≥99%), kerosene, Sudan III, methylene blue, petroleum ether, anhydrous ethanol, Span 20, Span 60, Span 80, AOT and dehydrated crude oil supplied by Shengli Oilfield. All reagents except the crude were analytical grade and purchased from either Macklin or Aladdin Biochemical.

2.4.2. Apparatus

The experimental apparatus consisted of inverted microscope (Leica DMi8, Germany) equipped with a high-speed camera (Photron, SA-Z, Japan), a precision syringe pump (Harvard

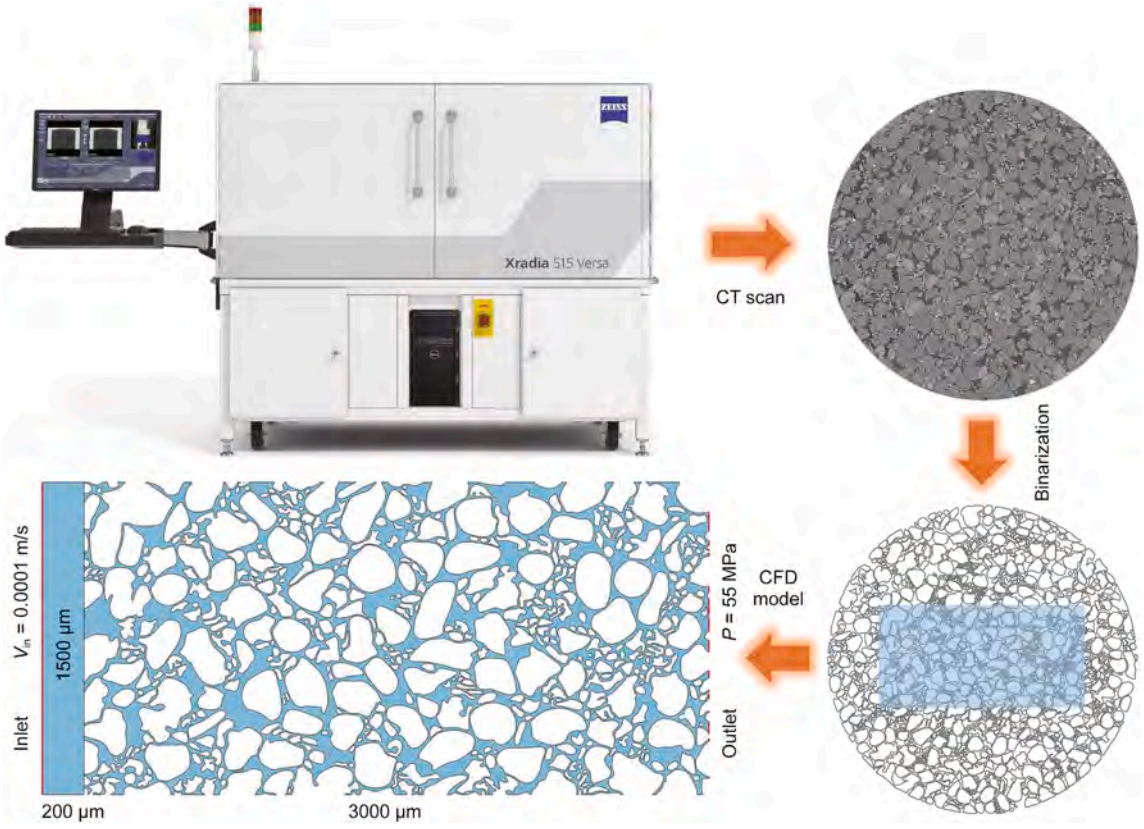


Fig. 3. Construction process of the porous media model.

Apparatus, PHD, 2000; USA) and two microfluidic chips. One chip was made of Polymethyl Methacrylate (PMMA) and featured a 300 μm main channel connected to a 200 μm side channel and a 100 μm blind-end pore; the right end served as the inlet, while the left end provided outlets for both the side channel and the blind-end pore (Fig. 4). The second chip was etched in glass and represented a porous medium (overall 45 mm × 45 mm) with pore-throat diameters ranging from 20 to 80 μm; the inlet was located at the lower right corner and the outlet at the upper left corner (Fig. 4).

2.4.3. Experimental procedure

Prior to each experiment, the working fluids were carefully prepared. Deionized water was dyed with 0.25 wt% methylene blue. Both n-octane and simulation oil were formulated with 0.5 wt% of Span 20, Span 60, Span 80 or AOT, while additive-free fluids served as blank controls. The n-octane was additionally stained with 0.25 wt% Sudan III to enhance phase contrast, whereas the black simulated oil required no dye. The microfluidic chips were first flushed with petroleum ether to remove oil and organic contaminants, then rinsed with anhydrous ethanol to eliminate water-soluble residues, and finally washed with deionized water and dried under a CO_2 stream.

For the PMMA chip, the pore was fully saturated with oil at an injection rate of 1 μL/min, after followed by CO_2 injection at the same rate until breakthrough. Recovery efficiency was determined by quantifying the residual oil film thickness on the pore walls and the fraction trapped in the blind-end pores. Each chemical additive

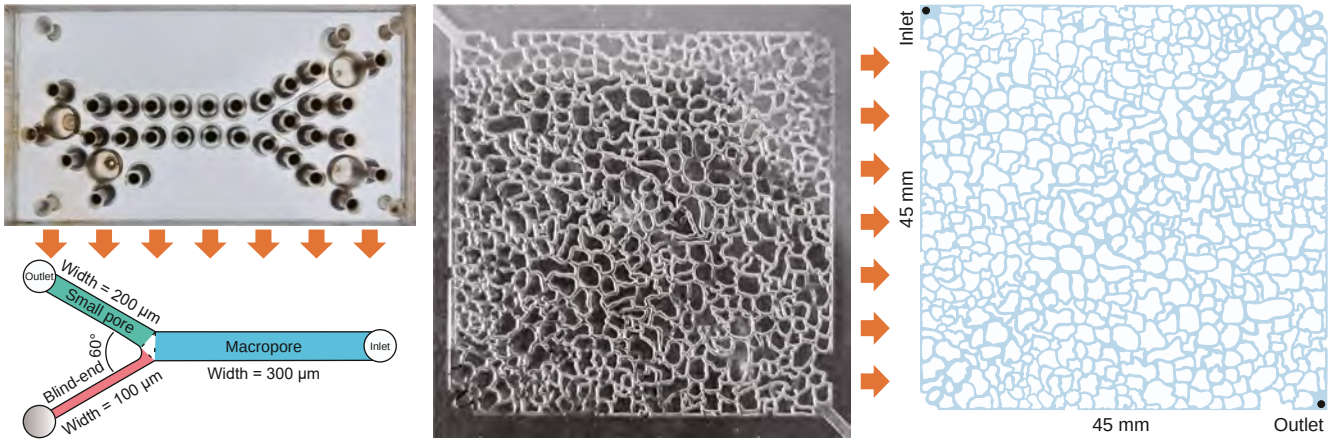
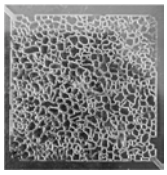


Fig. 4. Microfluidic chips used the experiments.

Table 1
Experiment scheme of the microscopic seepage experiments.

Experiment scheme	Chemicals	Oil	Gas	Microfluidic chip
①	—	Simulated oil	CO_2	
②	0.5% Span 20			
③	0.5% Span 60			
④	0.5% Span 80			
⑤	0.5% AOT			
⑥	—	C8		
⑦	0.5% Span 20			
⑧	0.5% Span 60			
⑨	0.5% Span 80			
⑩	0.5% AOT			

was tested in duplicate. For the etched-glass chip, deionized water was first injected, followed by n-octane at 2 μL/min, CO_2 was then injected at 2 μL/min until breakthrough. The oil recovery factor was calculated based on the areal distribution of the colored phases. All experiments were repeated for each chemical formulation, with the detailed experimental scheme provided in Table 1.

3. Results and discussion

3.1. Miscibility of CO_2 with oil

3.1.1. Miscibility process

The miscibility process between CO_2 and oils with different carbon chain lengths (C4, C8, and C12) at 388.15 K and 55 MPa was investigated using molecular simulations. Fig. 5 illustrates the dynamic evolution of miscibility in the C8 system. Initially, CO_2 and C8 molecules are segregated on the right and left sides of the pore, respectively. As the simulation proceeds, the interfacial region gradually diffuses, as evidenced by the simultaneous increase in C8 molecules within the CO_2 phase and CO_2 molecules within the C8 phase, eventually reaching dynamic equilibrium. Notably, significant differences were observed in the kinetics of approaching miscible equilibrium among oil systems with different chain lengths (Appendix A Figs. S1 and S2).

To quantitatively characterize the miscibility kinetics, the temporal evolution of relative component concentrations was analyzed for the C8-CO_2 system. It should be noted that incomplete pore filling after geometric optimization led to a transient increase in concentration at both sides during the early stages of the simulation (Fig. 6). However, after approximately 10 ps, the system exhibited typical miscible behavior: the concentrations of oil components in the CO_2 phase and CO_2 in the oil phase increased monotonically until reaching a stable state. Comparative analysis revealed that the rate of concentration increase became significantly slower with increasing oil chain length (Appendix A Figs. S3 and S4). This indicates that CO_2 interacts more strongly with lighter components (e.g., C4) under the same temperature and pressure conditions, thereby facilitating faster achievement of miscibility.

To quantify the effect of chemical agents on the miscibility between C8 and CO_2, the relative concentration distributions in both phases were statistically analyzed at equilibrium under different chemical conditions. The results show that, compared with the chemical-free system, the concentrations of C8 in the CO_2 phase and CO_2 in the C8 phase both increased significantly after the addition of chemicals (Fig. 7), indicating enhanced miscibility. Further analysis reveals that the chemical agents increased the average concentrations of C8 in the CO_2 phase and CO_2 in the C8 phase, although their effects differed. Span 20 primarily increased the concentration of C8 in the CO_2 phase, whereas AOT more effectively enhanced the concentration of CO_2 in the C8 phase. These findings suggest that Span 20 preferentially promotes the migration of C8 molecules into the CO_2 phase (extraction effect), while AOT strengthens the dissolution of CO_2 into the C8 phase.

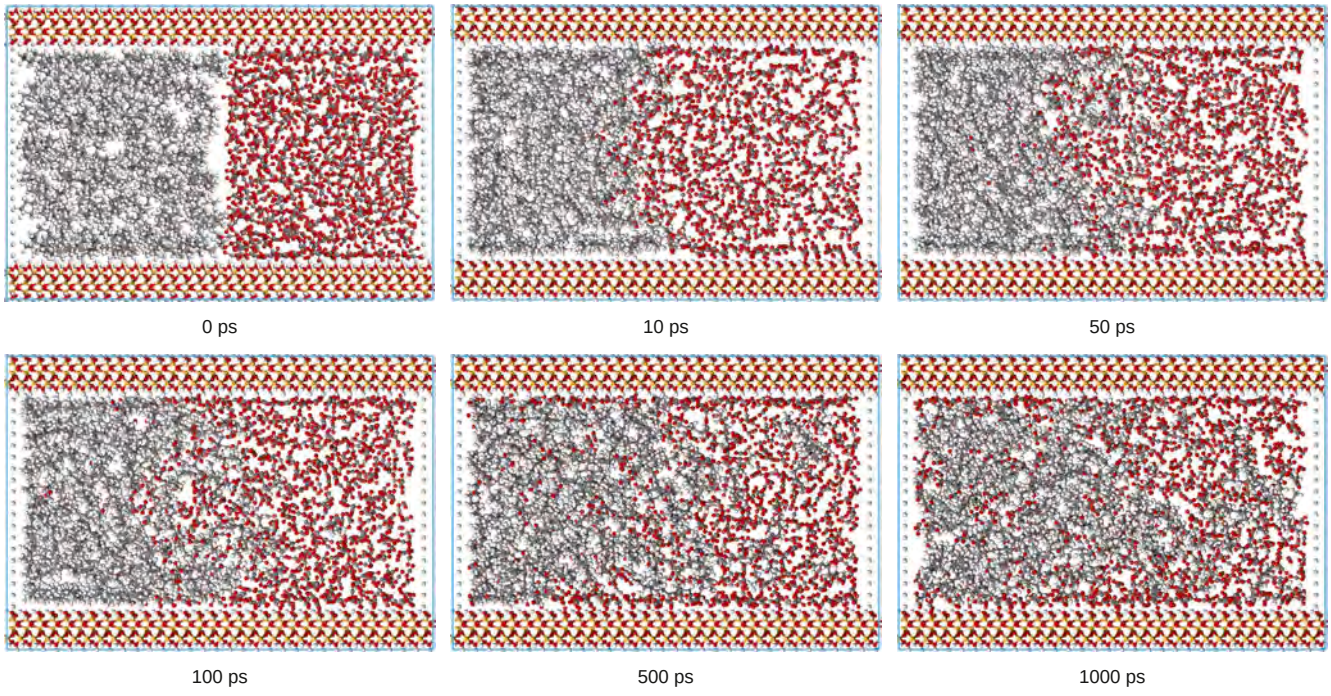


Fig. 5. The miscible process of CO_2 and C8.

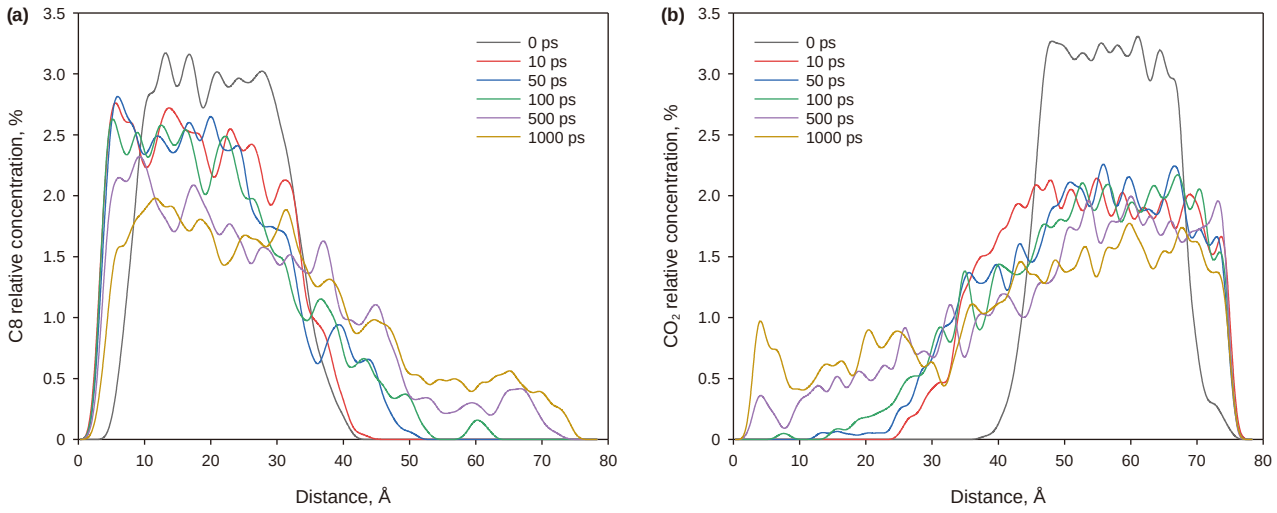


Fig. 6. The relative concentration of molecules in the C8-CO_2 system at different times. **(a)** The relative concentration of C8; **(b)** the relative concentration of CO_2.

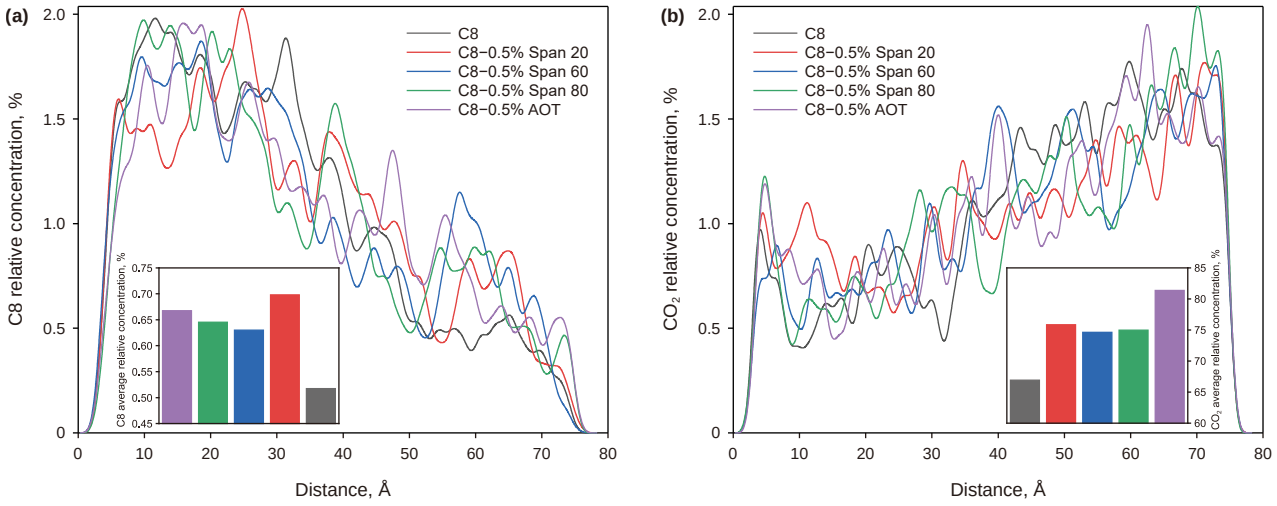


Fig. 7. Relative concentrations of C8 and CO_2 in the presence of different chemicals at the end of simulation. **(a)** Relative concentration of C8; **(b)** relative concentration of CO_2.

3.1.2. Miscible degree

To quantitatively evaluate the effect of chemical agents on CO_2-oil miscibility, this study proposes a novel quantitative characterization method for the miscibility degree. This approach utilizes statistical features of the relative CO_2 concentration distributions and defines the miscibility degree as the difference between the 75th percentile (Q_3) and the 25th percentile (Q_1) values. The procedure involves: (1) statistical analysis of CO_2 relative concentration distributions at different simulation timesteps; (2) determination of Q_3 and Q_1 for each timestep; (3) calculation of the interquartile range in relative concentration; and (4) normalization relative to the initial state (with the miscibility degree defined as 0 at $t = 0$). Compared with existing methods (Lv et al., 2023), this approach offers enhanced robustness by effectively mitigating the interference from outliers. The miscibility degree index for quantitatively characterizes CO_2-oil miscibility at the microscale is defined as:

$$M = 1 - \frac{R_{3/4,i} - R_{1/4,i}}{R_{3/4,0} - R_{1/4,0}} \times 100\% \quad (16)$$

where $R_{3/4,i}$ and $R_{1/4,i}$ denote the 75th and 25th percentiles of the CO_2 relative concentration distribution at time i, respectively; $R_{3/4,0}$ and $R_{1/4,0}$ represent the corresponding initial values at $t = 0$.

Similar characterization methods have been successfully applied and validated in previous studies. Researchers have used indices similar to the one proposed here to quantify the miscibility degree between CO_2 and crude oil, with good agreement between calculated results and experimental data (Wang et al., 2023; Lv et al., 2023). This method is not only applicable to CO_2-alkane systems but has also been successfully extended to CO_2-actual crude oil systems. Even in the presence of chemical additives, the calculated miscibility degrees showed strong consistency with experimental observations, confirming the universality of this index across different CO_2-crude oil systems. The miscibility degree increased with simulation time for all oil types. However, CO_2 exhibited significantly higher miscibility with light oil than with medium or heavy oils (Fig. 8(a)), indicating its preferential miscibility with lighter components. To improve miscibility with long-chain hydrocarbons, C8 was selected as a model system to evaluate four chemical agents (Span 20, Span 80, Span 60, and AOT) at

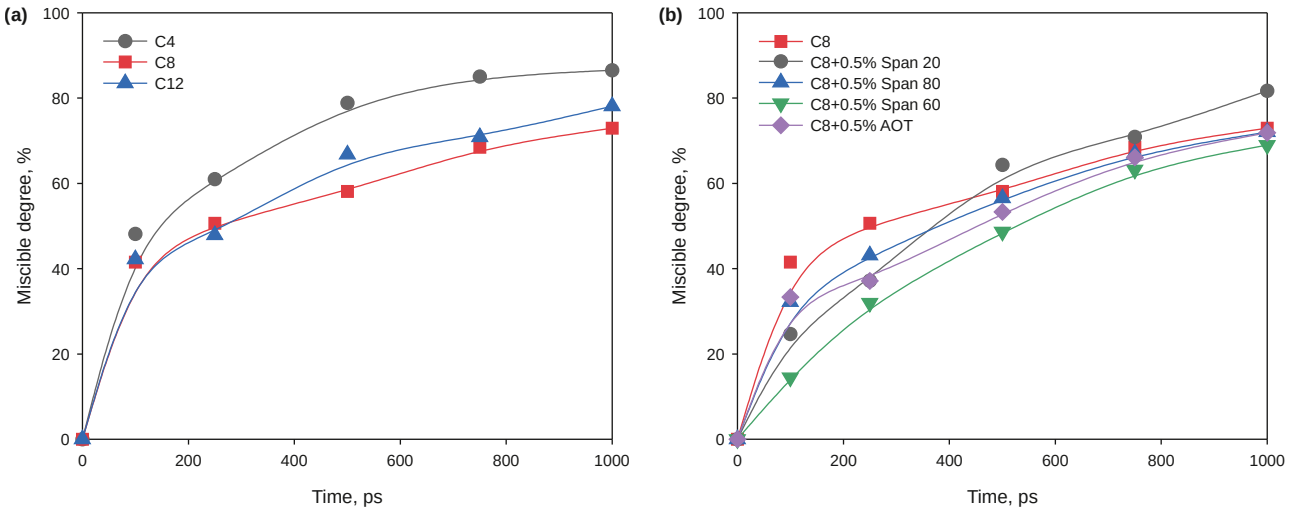


Fig. 8. Miscibility of CO_2 and oil in different systems. **(a)** Miscibility of CO_2 with different oils; **(b)** miscibility of CO_2 with C8 under different chemical agent conditions.

a concentration of 0.5 wt%. The miscibility degree analysis demonstrated that Span 20 provided the most substantial enhancement in CO_2-C8 miscibility within the simulated timeframe, while other surfactants showed limited effects (Fig. 8(b)). Consequently, Span 20 was selected for subsequent concentration optimization studies.

3.2. Mechanism of action of chemical agents

3.2.1. Dissolution

To quantitatively characterize the dissolution behavior of CO_2 in different oils, the temporal evolution of the total number of CO_2 molecules and the number of CO_2 molecules dissolved in the oil phase was statistically analyzed. The solubility of CO_2 in oil was defined as:

$$S_{CO_2} = \frac{N_{oil-CO_2}}{N_{t-CO_2}} \tag{17}$$

where S_{CO_2} represents the solubility of CO_2 in oil; N_{oil-CO_2} is the number of CO_2 molecules in the oil phase; and N_{t-CO_2} is the total number of CO_2 molecules in the pore.

This study quantitatively analyzed the dissolution characteristics of CO_2 in C4, C8, and C12 oil systems by tracking the number of CO_2 molecules within the oil phase over simulation time. The results reveal significant differences in dissolution behavior: CO_2 exhibited the highest solubility in light component C4, with an average solubility of 35.34%, while showing comparable dissolution capacities in the C8 and C12 systems (Fig. 9(a)). Chemical additives influenced CO_2 dissolution to varying degrees. In the C8 system, Span 60 and Span 80 increased CO_2 solubility by approximately 19%, whereas Span 20 and AOT showed negligible effects. Notably, although 0.5 wt% Span 20 delayed the dissolution process during the initial 500 ps, the final solubility reached levels comparable to the additive-free control (Fig. 9(a)). Systematic investigation of Span 20 concentration effects demonstrated that all concentrations except 0.5 wt% enhanced CO_2 dissolution, with 0.1 wt% providing the most significant improvement (a 20.64% increase in solubility) (Fig. 9(b)). These findings indicate that 0.1 wt% Span 20 as the optimal concentration for enhancing CO_2 dissolution in the C8 systems.

3.2.2. Extraction

To quantitatively characterize the extraction capacity of CO_2 for oil, the temporal evolution of the total number of oil molecules

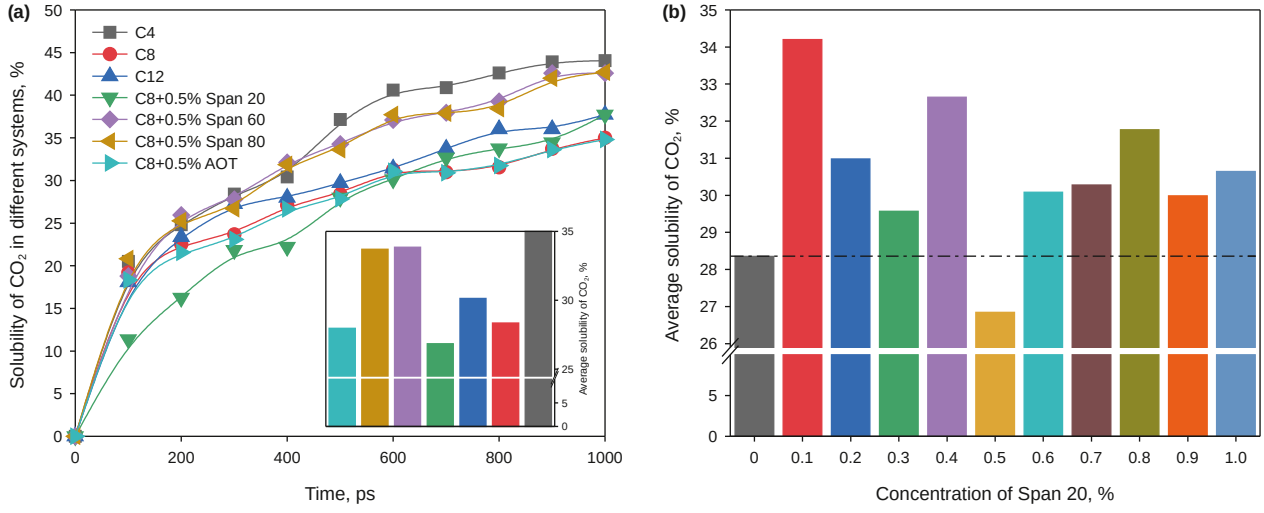


Fig. 9. Effect of chemicals on the solubility of CO_2 in C8. **(a)** Solubility of CO_2 under different chemical conditions; **(b)** average solubility of CO_2 at different Span 20 concentrations.

and the number of oil molecules entering the CO_2 phase was tracked. The extraction efficiency was defined as:

$$E_{oil} = \frac{N_{CO_2-oil}}{N_{t-oil}} \quad (18)$$

where E_{oil} represents the extraction efficiency of oil by CO_2; N_{CO_2-oil} is the number of oil molecules in the CO_2 phase; and N_{t-oil} is the total number of oil molecules in the pore.

This study systematically analyzed the extraction characteristics of CO_2 for oils with varying carbon chain lengths by monitoring the number of oil molecules within the CO_2 phase over simulation time. The results show that extraction efficiency is strongly component-dependent: CO_2 achieved an average extraction efficiency of 30.56% for the light component C4, while the efficiencies for C8 and C12 remained approximately 20% within the simulated timeframe (Fig. 10(a)). This confirms the preferential extraction of lighter components by CO_2. When chemical additives were introduced at 0.5 wt%, all agents enhanced the extraction efficiency of C8, albeit to different extents. Span 20 exhibited the largest improvement (27.3%), followed by Span 60 (25.46%) and AOT (23.03%), while Span 80 provided only limited enhancement (Fig. 10(a)). This indicates that Span 20 has superior efficacy in promoting C8 extraction at equivalent concentrations. Further concentration optimization revealed a clear concentration dependence for Span 20: concentrations below 0.8 wt% universally enhanced extraction, whereas 0.8 wt% and 0.9 wt% resulted in a notable reduction. Importantly, 0.5 wt% Span 20 yielded the greatest improvement in extraction efficiency, increasing it by 44.60% compared with the additive-free system (Fig. 10(b)). These results provide valuable guidance for the selection of optimal chemical concentrations in field applications.

3.2.3. Diffusion

To eliminate the influence of initial system non-equilibrium, the latter 80% of simulation time was selected for diffusion coefficient calculations. The results indicate minimal variation in CO_2 diffusion coefficients across different oil systems and chemical agents, with values consistently around 0.6×10^{-8} m^2/s (Fig. 11(a)). Notably, only 0.1 wt% Span 20 significantly enhanced CO_2 diffusion in the C8 system, increasing the diffusion coefficient by 12.38% (Fig. 11(b)). Experimental studies have shown that CO_2 diffusion coefficients in crude oil increase rapidly with pressure in the lower pressure ranges but tend to stabilize at higher pressures (Li et al., 2016). Based on experiment data from this reference, a logarithmic fitting relationship was established, yielding a diffusion coefficient of 0.176×10^{-8} m^2/s at 55 MPa (Fig. 12(a)). This value differs significantly from the simulation results due to fundamental differences in the models: the simulations employed an ideal pore model, whereas experimental data were obtained from actual core samples with complex geometric features and tortuosity, which are factors known to strongly influence fluid diffusion (Gao et al., 2019). Specifically, CO_2 diffusion coefficients in cores with a tortuosity of 1.87 were approximately 25 times higher than those in cores with tortuosity of 5.39 (Fig. 12(b)). In addition, the CO_2 diffusion coefficients in different alkane components calculated from molecular simulations were compared with publicly reported experimental data (Table 2). The comparison shows that the diffusion coefficients obtained in this study are of the same order of magnitude as those reported for light to medium crude oil systems, with consistent trends. For heavy oil-asphaltene systems, the diffusion coefficients are markedly lower due to higher viscosity, which aligns well with the physical trends observed in this study. Literature data under varying pressure, temperature, and viscosity conditions further confirm that the simulation method and parameter calculations presented here are consistent with general experimental and field observations. This validates the rationality and reliability of the cross-scale parameter transfer within the multiscale coupling framework.

3.2.4. Interaction

To elucidate the mechanism of chemical agents, the interaction energy between CO_2 and different oil systems was calculated. The analysis shows that interaction energies increased with simulation time in all systems, eventually approaching equilibrium (Fig. 13). Notably, the interaction energy between CO_2 and the light component C4 was significantly higher than those for the C8 and C12 systems. This provides molecular-scale evidence for the preferential interaction of CO_2 with lighter components and its efficient extraction of such fractions. These simulation results are consistent with previous observations in which C8, C12, and C16 were used to represent light, medium, and heavy oils, respectively. Those studies reported that the absolute value of interaction energy decreased with increasing hydrocarbon chain length (Liu et al., 2024). This agreement confirms that lighter components exhibit stronger molecular-scale interactions with CO_2, offering

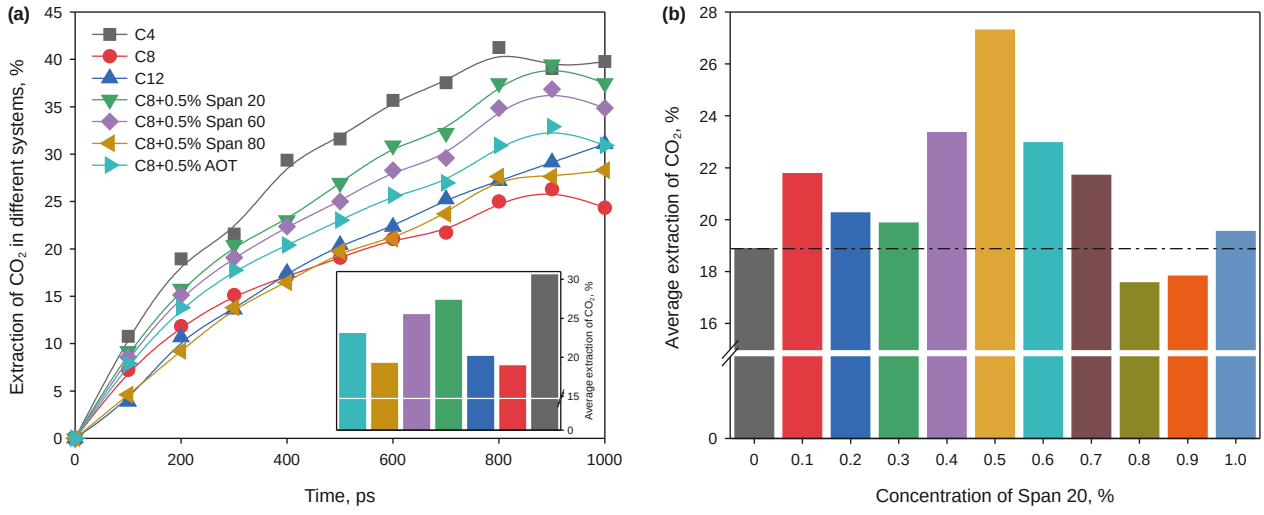


Fig. 10. Effect of chemicals on CO_2 extraction rate. **(a)** CO_2 extraction rate from oil in different systems; **(b)** average CO_2 extraction rate from C8 in different Span 20 concentrations.

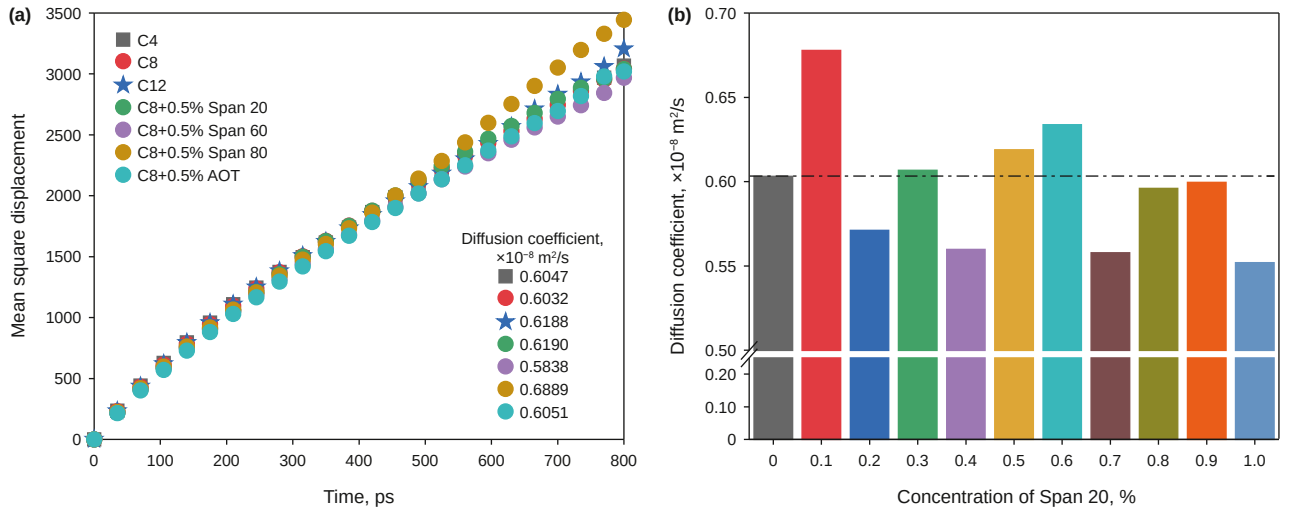


Fig. 11. Diffusion coefficients of CO_2 in different systems. **(a)** Diffusion coefficients of CO_2 in different oils and chemicals; **(b)** diffusion coefficients of CO_2 in C8 at different Span 20 concentrations.

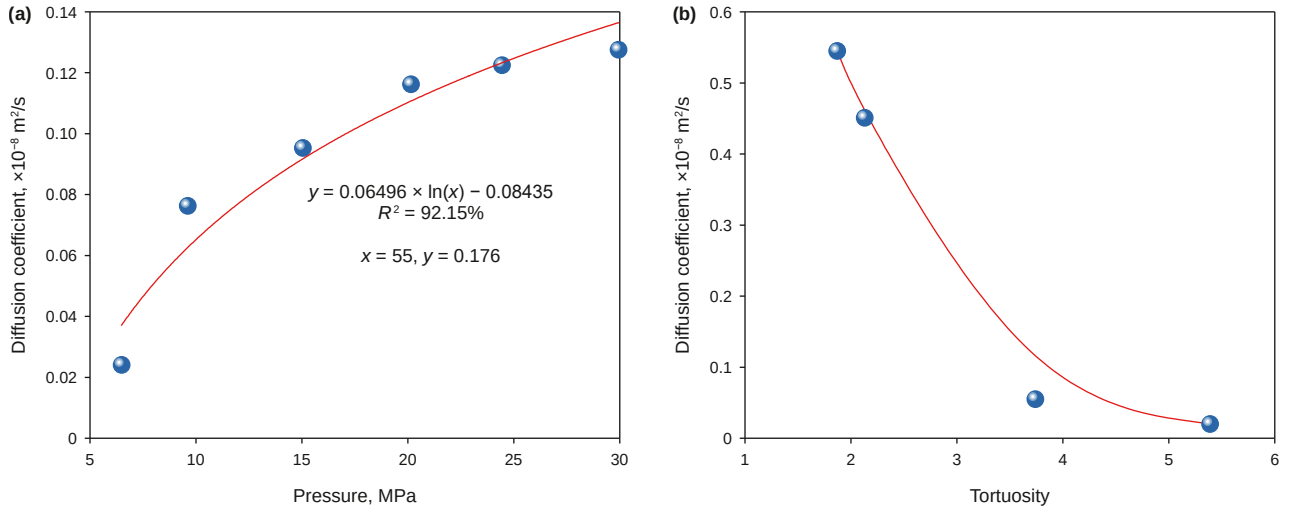


Fig. 12. Factors affecting CO_2 diffusion coefficient. **(a)** Effect of pressure on CO_2 diffusion coefficient (Li et al., 2016); **(b)** effect of tortuosity on CO_2 diffusion coefficient (Gao et al., 2019).

Table 2
The comparison of diffusion coefficients between this study and experimental conditions.

Type of oil	Pressure, MPa	Temperature, K	Viscosity, mPa·s	Diffusion coefficient, × 10^{-8} m^2/s	Source
Butane	55.00	388.15	0.140 (388.15 K)	0.8513	This study (Molecular simulation)
Octane			0.285 (388.15 K)	0.6592	
Dodecane			0.406 (388.15 K)	0.6505	
Bitumen	4.00	363.15	767 (368.15 K)	0.0470	Upreti and Mehrotra (2000)
Heavy oil	3.50	294.55	12,854 (294.55 K)	0.0430	Zheng et al. (2016)
Decane	6.00	308.15	—	0.4580	Liu et al. (2016)
Light oil	29.94	403.15	10 (353.15 K)	0.1276	Li et al. (2016)
Light oil	14.56	298.15	7.26 (323.15 K)	0.6704	Li et al. (2018)
Light oil	30.00	353.15	1.23 (353.15 K)	0.5450	Gao et al. (2019)
Heavy oil	5.00	393.15	179 (294.15 K)	0.5778	Zhou et al. (2020)
Medium oil	2.82	323.15	5.00 (323.15 K)	0.4000	Ssebadduka et al. (2020)
Paraffin	9.00	313.75	0.012 (313.75 K)	0.1000	Liu et al. (2022b)

theoretical insights into the selective extraction mechanisms during CO_2 flooding. Furthermore, recent experimental studies provide strong support for the present simulation results (Wang et al., 2023; Li et al., 2023a). The experiments demonstrated that the addition of surfactants can significantly reduce the interfacial tension between CO_2 and crude oil and shift the wettability from

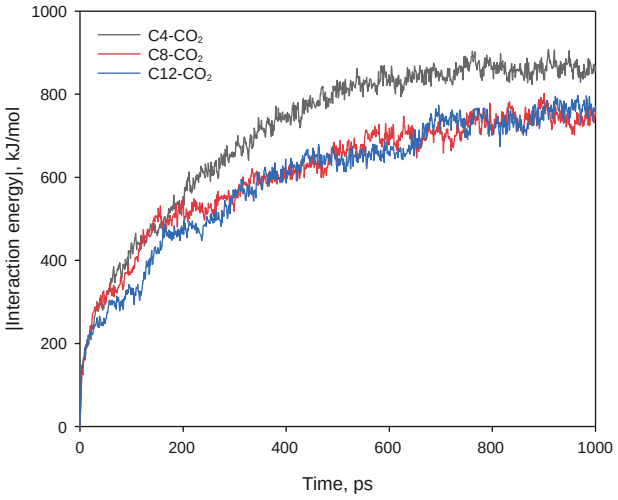


Fig. 13. Interaction energy of CO_2 with different oil.

oil-wet to CO_2-wet, thereby quantitatively confirming the ability of chemical agents to reduce interfacial resistance and eliminate oil adhesion on pore walls.

Studies have shown that when CO_2 and crude oil have comparable molecular weights, their intermolecular interactions may not dominate factor controlling miscibility behavior (Wang et al., 2021). Consequently, the interaction energy between oil and pore walls was calculated. The results demonstrate that all chemical additives reduced the interaction energy between the pore walls and C8, with 0.5 wt% AOT producing the most significant reduction (Fig. 14). In the AOT system, molecular distribution analysis revealed that AOT molecules preferentially accumulated near the pore walls after being added to the CO_2-C8 system (Fig. 15). The unique amphiphilic structure of AOT, which contains both hydrophobic and hydrophilic groups, promotes its accumulation at the interface, effectively weakening the oil-wall interactions. Experimental results further confirm that the addition of AOT enables more effective stripping of crude oil from the pore walls, thereby improving recovery (Fig. 28). These findings verify that chemical agents enhance oil recovery by reducing adhesion

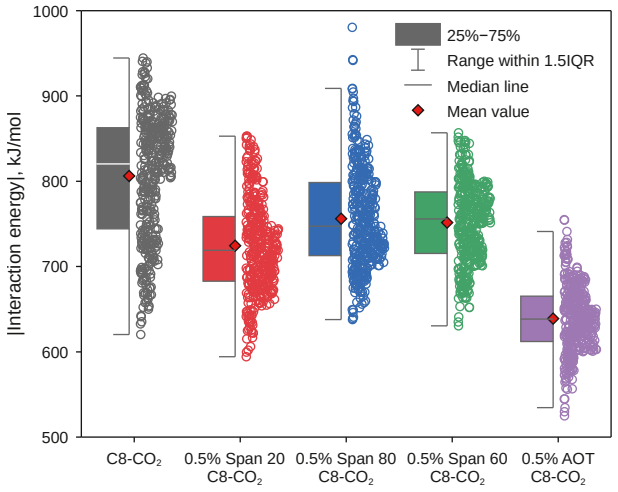


Fig. 14. The interaction energy between C8 and pore wall under different chemical conditions.

forces between the oil and pore walls, thereby promoting the desorption of adsorbed crude oil. Overall, this study provides molecular-level insights into chemically enhanced recovery mechanisms and offers potential solutions to the challenges identified by Huang et al. (2024), specifically the thickening of the adsorbed oil layer and the resulting reduction in effective pore volume during reservoir depressurization.

To further investigate the concentration-dependent effect of Span 20 on oil desorption, the interaction energy between C8 and pore walls was systematically evaluated across a range of Span 20 concentrations (Appendix A Fig. S5). Statistical analysis of average interaction energies at different concentrations (Fig. 16) reveals that Span 20 consistently reduced the C8-wall interaction energy, exhibiting a clear concentration dependence. Importantly, the minimum average interaction energy occurred at 0.2 wt% Span 20, indicating optimal oil-stripping efficacy at this concentration. These findings establish 0.2 wt% Span 20 as the theoretically optimal concentration for field applications, as it maximizes the desorption of adsorbed crude oil from pore walls and thereby enhance oil recovery.

3.3. Microscopic seepage

To investigate pore-scale effects of chemical agents on CO_2 flooding, this study developed a microscopic oil displacement model that incorporates the chemical mechanisms of chemical assistance. The model integrates the modifications induced by chemical agents on CO_2 dissolution, extraction efficiency, and diffusion behavior, thereby enabling accurate characterization of microscopic seepage patterns during chemical-assisted CO_2 flooding.

3.3.1. CFD simulation parameters

Key physical properties, including viscosity and density of CO_2 and oil under reservoir conditions, as well as the molar mass and density of chemical agents, were determined through theoretical calculations (Table 3). These parameters served as essential inputs for the CFD simulations. Fluid-wall interactions were governed by wall boundary conditions: no-slip conditions represent intermediate wettability, positive slip values correspond to water-wet conditions, and negative slip values indicate oil-wet conditions (Vinogradova, 1995). Accordingly, the chemical-free CFD model employed no-slip boundary conditions, while systems containing chemical additives adopted positive-slip conditions. To quantitatively incorporate the chemical effects, a reaction source term was introduced into the CFD model based on the molecular simulation results. This term was used to simulate the influence of chemical agents on CO_2 dissolution and extraction in oil. Relative to the chemical-free baseline (defined as 100%), values of solubility or extraction efficiency greater than 100% indicates enhancement, while values below 100% indicate inhibition. Simulations confirmed that all tested chemicals improved CO_2 dissolution capacity and extraction efficiency. The effects of chemicals on CO_2 solubility and the corresponding model fittings are shown in Fig. 17, while their effects on extraction processes are presented in Fig. 18.

3.3.2. Influencing factor

Seven CFD simulation cases were designed to investigate the effects of different oils and chemical agents on microscopic seepage characteristics (Table 4). C4, C8, and C12 were selected to represent light, medium, and heavy oils, respectively. Chemical agents included 0.5 wt% Span 20, Span 60, Span 80 (non-ionic surfactants), as well as AOT (anionic surfactant). This design

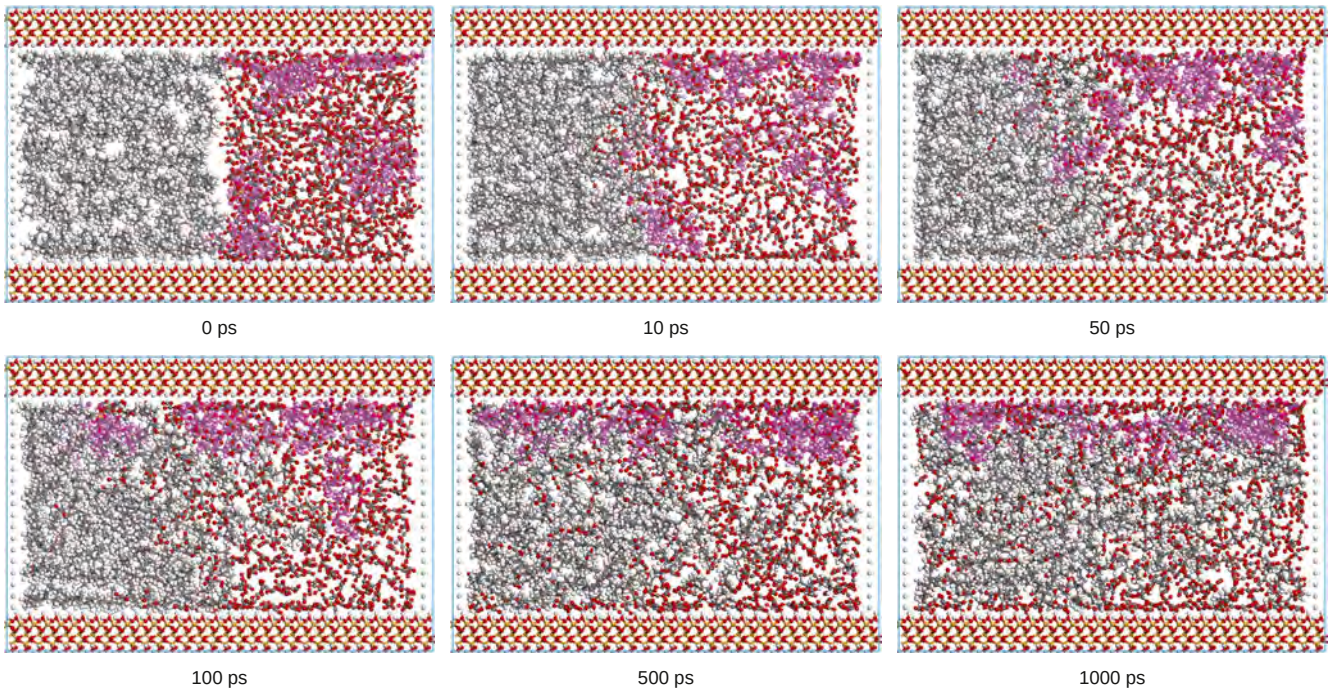


Fig. 15. The miscible process of CO_2 and C8 under 0.5% AOT.

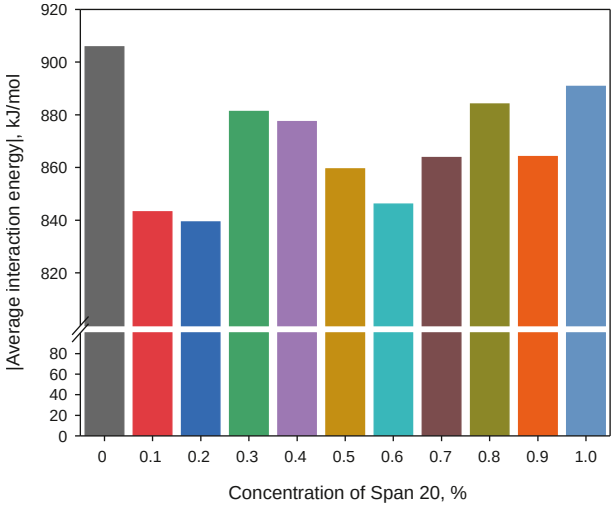


Fig. 16. The average interaction energy between C8 and pore wall under different Span 20 concentrations.

enables a systematic evaluation of how different surfactant types regulate microscopic seepage behavior across oil compositions of varying molecular weights.

3.3.2.1. Oil type. The microscopic flow behavior of C4, C8, and C12 oils during CO_2 flooding was simulated using schemes ①, ②, and ③. To comprehensively characterize fluid distribution dynamics, snapshots of oil and CO_2 distributions at nine selected time points were captured for each scheme (Appendix B Figs. S1–S6). Specifically, Figs. S1, S2, and S3 in Appendix B illustrate the microscopic seepage processes for C4, C8, and C12, respectively, while Figs. S4, S5, and S6 show the corresponding CO_2 flow behaviors. Given the large number of snapshots, the characteristic distributions at 7 s were selected for comparative analysis (Figs. 19 and 20). Fig. 19 presents the oil distributions for different oils, and Fig. 20 shows CO_2 distributions under the corresponding conditions. Initially, the porous medium was fully saturated with oil (red). During flooding process, the color gradient from red to blue visually represents the progressive miscibility between CO_2 and oil (Fig. 19). The results indicate that oil preferentially flowed through larger pore channels, while residual oil primarily remained in small pore and blind-end. Moreover, the amount of residual oil increased significantly with longer carbon chain length. The CO_2 distribution characteristics (Fig. 20) revealed superior miscibility with lighter oils, which is consistent with the recovery statistics. Oil displacement efficiency increased progressively with decreasing carbon chain length (Fig. 23), confirming that lighter components are more readily produced in CO_2 miscible flooding.

Table 3
Fundamental fluid properties of CFD simulation.

Materials	Molar mass, g/mol	Density, g/cm^3	Viscosity, mPa·s
C4	58.14	0.6161	0.1400
C8	114.26	0.6747	0.2850
C12	170.34	0.6671	0.4060
CO_2	44.01	0.8229	0.0734
AOT	444.56	1.1	—
Span 20	346.46	1.1	—
Span 60	430.62	1.1	—
Span 80	428.6	1.1	

3.3.2.2. Chemical agent type. The microscopic flow processes under chemical additive schemes ④, ⑤, ⑥, and ⑦ were simulated, with oil and CO_2 distribution characteristics captured at multiple time points. For comparative analysis, the distributions at 7 s under different chemical conditions were selected (Figs. 21 and 22). The results show that all chemical additives significantly reduced residual oil saturation and accelerated the miscibility process between CO_2 and C8. Among the four chemical agents, the anionic surfactant AOT exhibited the least effective enhancement of

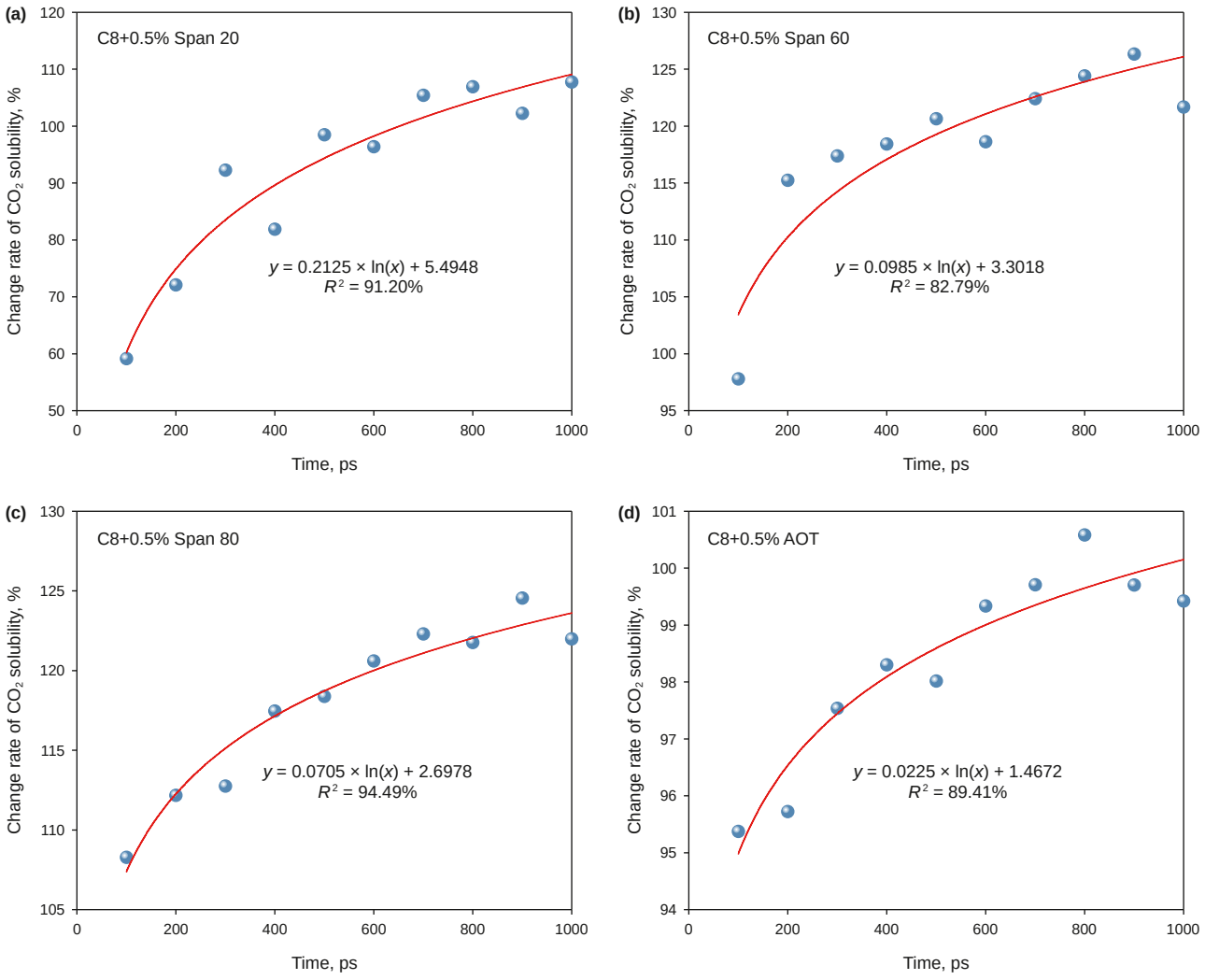


Fig. 17. Effect of different chemicals on the solubility of CO_2 in C8. **(a)** 0.5% Span 20 on the solubility of CO_2 in C8; **(b)** 0.5% Span 60 on the solubility of CO_2 in C8; **(c)** 0.5% Span 80 on the solubility of CO_2 in C8; **(d)** 0.5% AOT on the solubility of CO_2 in C8.

miscibility, leaving higher residual oil saturation in small pore and blind-end (Fig. 21). In contrast, among the non-ionic surfactants, Span 20 demonstrated superior performance in mobilizing oil trapped in small and dead-end pores, while Span 60 and Span 80 showed comparable enhancement effects. The CO_2 concentration distributions further revealed that Span 20 substantially improved CO_2 penetration into small pores and blind-end. Under AOT treatment, the CO_2 concentration within the oil phase was notably lower than that achieved with the other chemical agents (Fig. 22).

Subsequent statistical analysis of oil recovery across all simulation schemes revealed that, in the absence of chemical additives, the ultimate recovery for all oils failed to reach the theoretical maximum of 100% due to the intermediate wettability of the pore walls (Fig. 23). The addition of chemicals significantly improved oil displacement efficiency by altering rock wettability and regulating CO_2 dissolution, extraction, and diffusion within the oil phase. Comparative analysis showed notable differences in the performance of the chemical agents. Span 20 provided the greatest enhancement in oil recovery efficiency, followed by Span 60 and Span 80 with comparable effects, while AOT was the least effective (Fig. 23). These results indicate that non-ionic surfactants, particularly Span 20, effectively accelerate CO_2-oil miscibility, thereby enhancing both dissolution and extraction processes. The findings are consistent with experimental observations that non-ionic surfactants promote miscibility and modify wettability, with improved performance under HTHP conditions (Li et al., 2023a). Overall, the simulations validate the technical feasibility of chemical-assisted CO_2 flooding for the efficient development of deep reservoirs.

To quantitatively compare the recovery enhancement induced by chemical additives under simulated and experimental porous media conditions, the simulation snapshot shown in Fig. 21 was processed to calculate the corresponding oil recovery. The results show that Span 20 produced the largest increment, followed by Span 60 and Span 80 with similar improvements, while AOT was the least effective. Without chemical additives, the recovery was 54.31%. After the addition of Span 20, Span 60, Span 80, and AOT, the recovery increased 77.02%, 64.46%, 68.95%, and 40.57%, respectively (Fig. 24(b)). Experimentally, images captured at CO_2 breakthrough were analyzed to determine the recovery. In the absence of chemicals, the recovery was 20.32%. All surfactants increased this value, with Span 20 enabling CO_2 to invade a larger fraction of pores and yielding the greatest improvement. Span 60 and Span 80 provided comparable gains, whereas AOT was the least effective (Fig. 24(a)). The discrepancy between simulation and experiment is partly attributed to the differing abilities of the

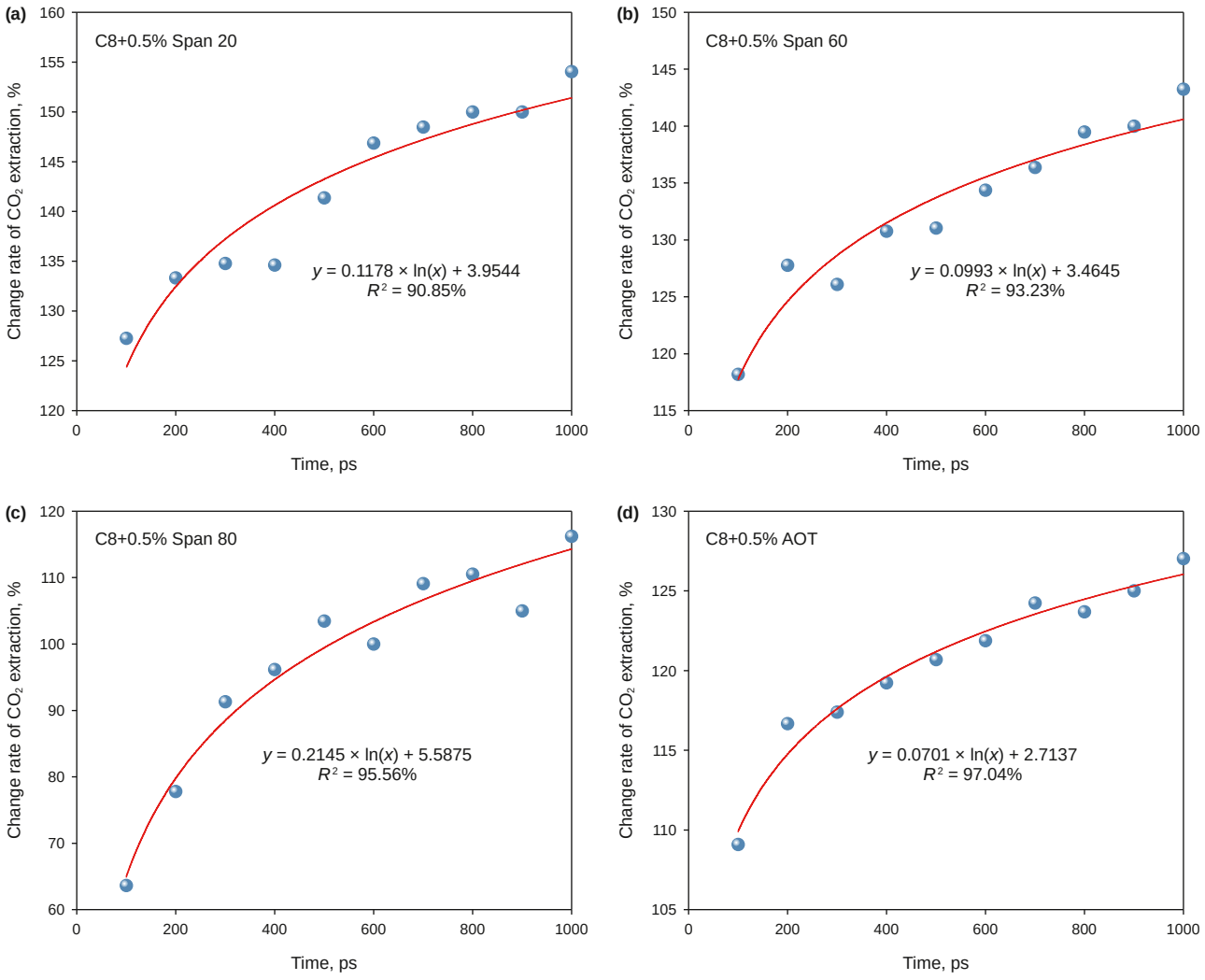


Fig. 18. Effect of different chemicals on CO_2 extraction in C8. **(a)** 0.5% Span 20 on CO_2 extraction in C8; **(b)** 0.5% Span 60 on CO_2 extraction in C8; **(c)** 0.5% Span 80 on CO_2 extraction in C8; **(d)** 0.5% AOT on CO_2 extraction in C8.

Table 4
CFD simulation scheme.

Simulation scheme	Injection medium	Oil	Diffusion coefficient, × 10^{-8} m^2/s
①	CO_2	C4	0.6047
②	CO_2	C8	0.6032
③	CO_2	C12	0.6188
④	CO_2 + 0.5% Span 20	C8	0.6190
⑤	CO_2 + 0.5% Span 60	C8	0.5838
⑥	CO_2 + 0.5% Span 80	C8	0.6889
⑦	CO_2 + 0.5% AOT	C8	0.6051

surfactants to detach oil films from pore walls. Span 20 consistently outperforms the other additives in macropore, small pore, and blind-end (Fig. 28). Overall, the comparison shows that the smallest discrepancy occurred for Span 20, and consistent trends were observed for the remaining surfactants (Fig. 24(b)).

3.3.2.3. Pore type. The oil recovery characteristics in different pore types (macropore, small pore, and blind-end) were monitored and analyzed (Figs. 25–27), with displacement efficiency quantitatively evaluated using the ratio of the area enclosed by recovery curves to the total coordinate area. The results indicate that in macropore, the oil displacement efficiencies for C4, C8, and C12 reached 83.56%, 80.10%, and 78.30%, respectively, with C4 exceeding C8 and C12 by 3.47% and 5.27%. After the addition of chemical agents, the recovery of C8 increased with all additives (Fig. 25). Specifically, Span 20 achieved the highest efficiency of 87.67%, followed by Span 60 (86.71%), Span 80 (86.98%), and AOT (85.58%). Overall, the chemical agents provided relatively limited enhancement in macropore. At a concentration of 0.5%, Span 20 improved the displacement efficiency by 7.57%, Span 60 by 6.62%, Span 80 by 6.88%, and AOT by 5.48%.

Systematic analysis of oil displacement efficiency in small pore was subsequently conducted (Fig. 26). The baseline displacement efficiencies for C4, C8, and C12 in small pore were 77.51%, 73.94%, and 72.00%, respectively, with C4 exceeding C8 and C12 by 3.57% and 5.51%. Chemical additives substantially enhanced the recovery of C8. Span 20 achieved the highest efficiency of 86.52%, followed by Span 60 (85.49%), Span 80 (85.80%), and AOT (84.19%). These data clearly demonstrate significant improvement in displacement efficiency within small pore for C8 under chemical treatment. At a concentration of 0.5%, the efficiency increased by 12.57% with Span 20, 11.54% with Span 60, 11.85% with Span 80, and 10.24% with AOT.

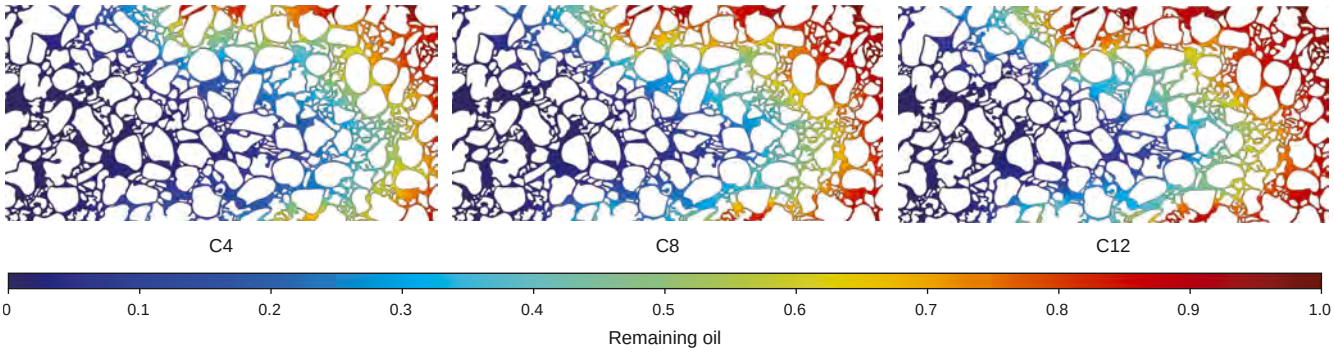


Fig. 19. Different oil distribution characteristics at 7 s.

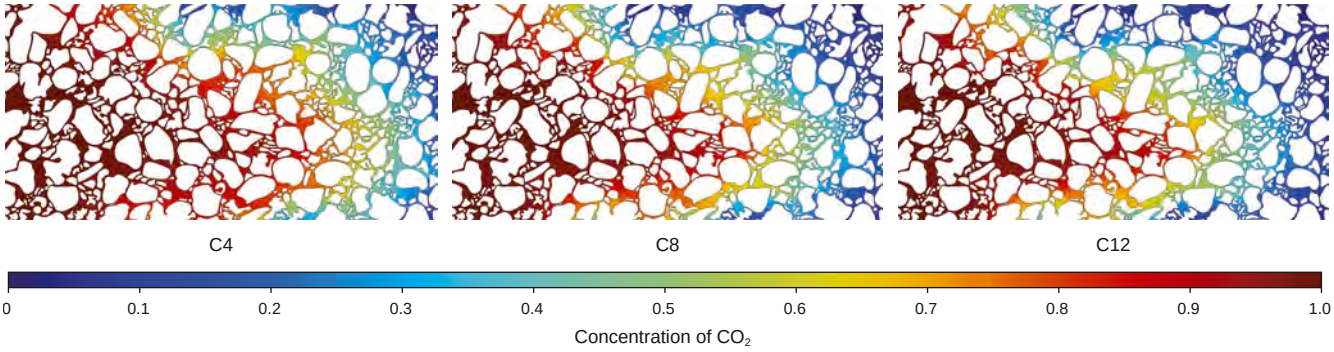


Fig. 20. The distribution characteristics of CO_2 in different oils at 7 s.

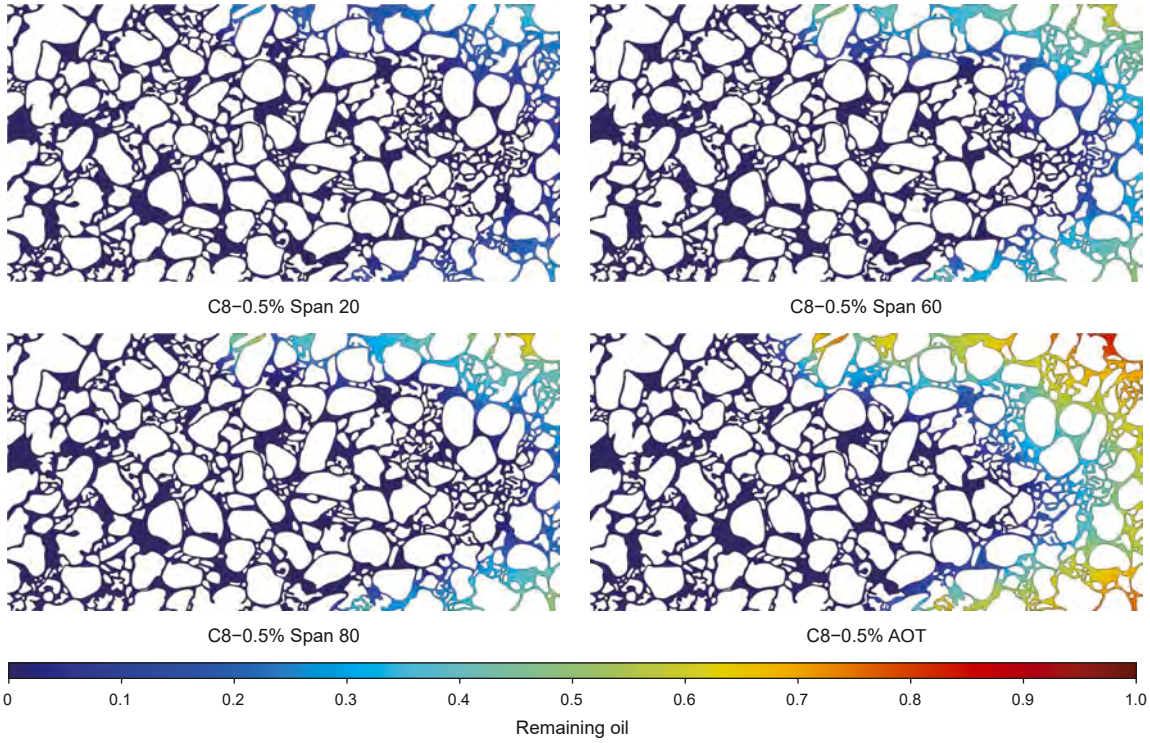


Fig. 21. The distribution characteristics of C8 under different chemical conditions at 7 s.

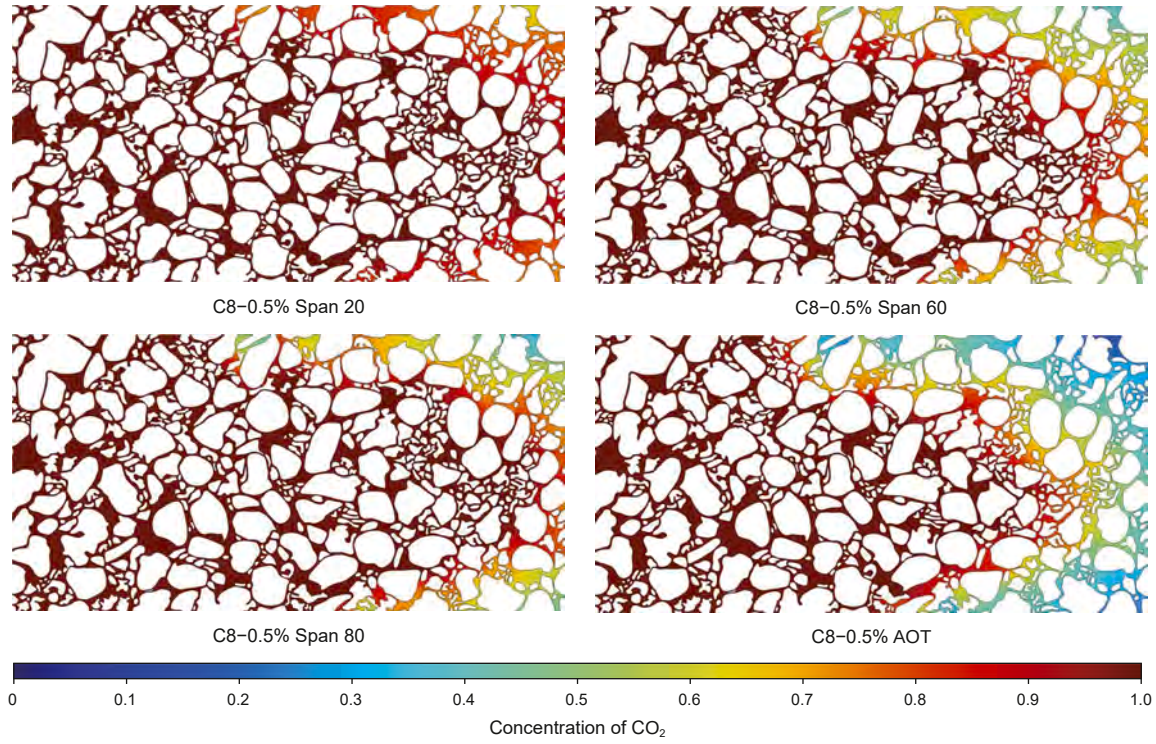


Fig. 22. The distribution characteristics of CO_2 under different chemical conditions at 7 s.

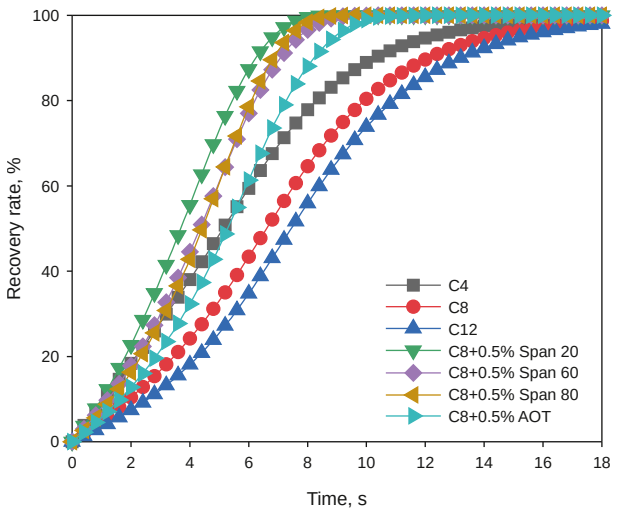


Fig. 23. Oil recovery under different schemes.

Analysis of oil displacement efficiency in dead-end concluded this section (Fig. 27). The baseline displacement efficiencies for C4, C8, and C12 in blind-end were 70.12%, 64.73%, and 62.19%, respectively, with C4 exceeding C8 and C12 by 5.39% and 7.93%. Chemical additives markedly enhanced the recovery of C8 in blind-end: Span 20 achieved 80.78% efficiency (a 16.05% increase), Span 60 reached 78.57% (a 13.84% increase), Span 80 attained 78.73% (a 14.00% increase), and AOT yielded 73.82% (a 9.09% increase). Notably, compared with macropore and small pore, Span 20 provided the most substantial enhancement in blind-end (16.05% increase), demonstrating its particular effectiveness in improving oil recovery from these challenging pore structures.

Microfluidic experiments corroborated the simulations results. Recovery factors obtained for individual pore types enabled a quantitative assessment of the chemical additives at the pore scale. Regardless of the additive used, oil recovery in macropore increased by approximately 8%. In small pore, Span 20 delivered the largest increment (12.7%), whereas the other surfactants enhanced recovery by approximately 9%. In blind-end, Span 20 increased recovery by 14.5%, Span 60 and Span 80 by 10.9% and 11.0%, respectively, and AOT by only 8.9% (Fig. 28(a)). The good agreement between the experimental and simulation results validates the predictive capability of the model for the chemically assisted displacement (Fig. 28(b)).

In summary, the differences in oil displacement efficiency among the tested oils became more pronounced as the pore type changed from macropore to small pore and then to blind-end. Specifically, the efficiency for C4 exceeded that for C12 by 5.27% in macropore, 5.51% in small pore, and 7.93% in blind-end, indicating that displacement efficiency consistently increases with decreasing carbon chain length across all pore types. At a chemical additive concentration of 0.5%, the recovery of C8 improved in all pore types, but degree of enhancement varied. Span-series surfactants performed best in blind-end, with Span 20 achieving the highest efficiency gain (16.05%). In contrast, AOT showed a distinct enhancement pattern: +5.48% in macropore, +10.24% in small pore, and +9.09% in blind-end. These findings suggest that Span-series surfactants preferentially enhance oil recovery in challenging pore geometries (small pores and blind-end), whereas AOT primarily improves efficiency in small pores.

3.3.3. Sensitivity analysis

To quantify the influence of key parameters on the performance of chemical-assisted CO_2 flooding, a sensitivity analysis was conducted based on the C8 + 0.5% Span 20 system, focusing on the diffusion coefficient, CO_2 solubility, extraction efficiency, and injection velocity. The results are shown in Fig. 29. The sensitivity

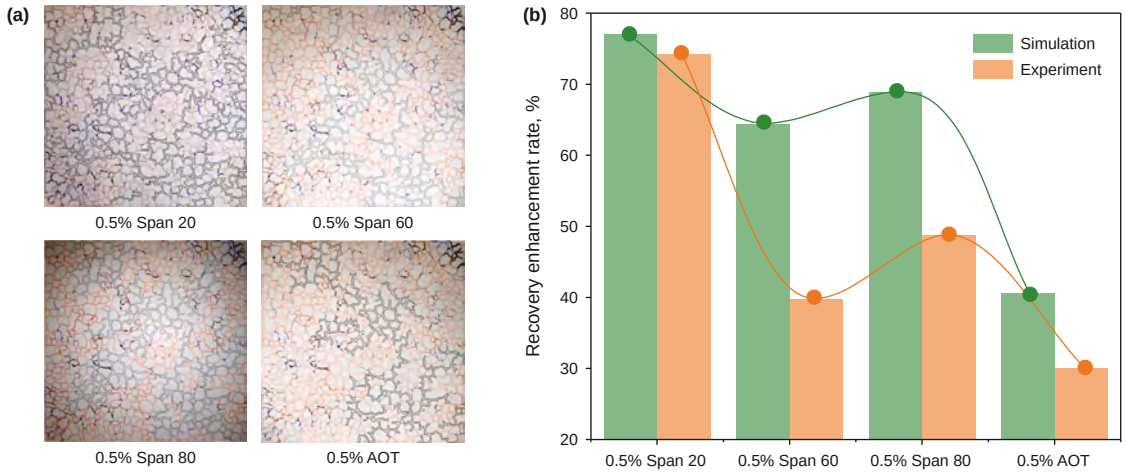


Fig. 24. Recovery under different chemical agent conditions. **(a)** Snapshot of experimental results; **(b)** comparison of experimental and simulation results.

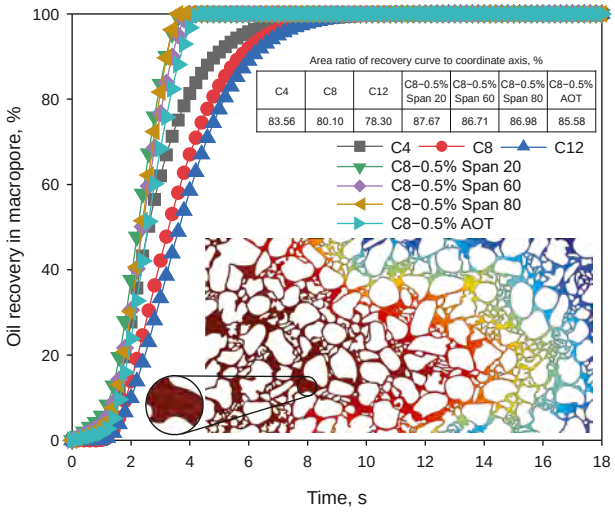


Fig. 25. Oil recovery in macropore under different schemes.

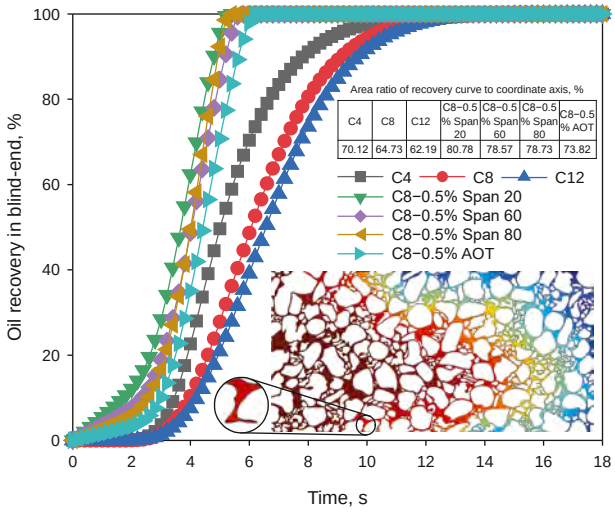


Fig. 27. Oil recovery in blind-end under different schemes.

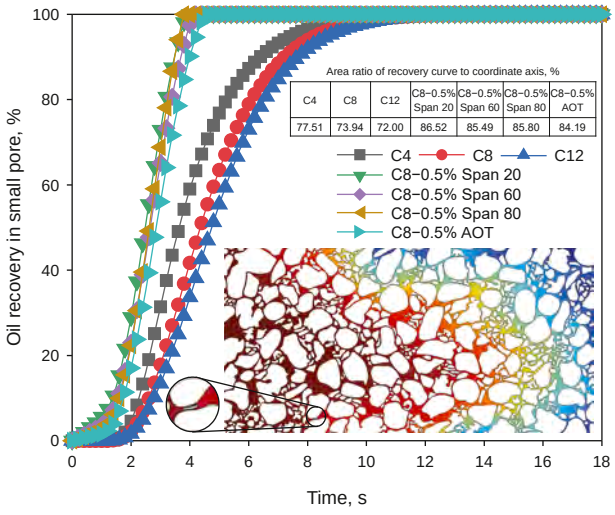


Fig. 26. Oil recovery in small pore under different schemes.

analysis of the diffusion coefficient shows that the peak of the recovery curve increases by approximately 1.0% with each doubling of the diffusion coefficient, indicating that under the current conditions the mass transfer efficiency has already approached its maximum, and thus its contribution to further enhancing oil recovery is relatively limited (Fig. 29(a)). The effect of CO_2 solubility exhibits a non-monotonic behavior. Within the initial 0–3 s, the recovery shows a brief negative fluctuation, and the negative trough deepens as the solubility increases. Subsequently, the recovery rapidly rebounds, reaching a positive peak within 4–6 s (with a maximum improvement of about 5%). This suggests that although high solubility may temporarily reduce displacement efficiency at an early stage, it significantly enhances recovery at a later stage (Fig. 29(b)). The improvement in recovery due to extraction efficiency is second only to that due to the injection rate, with a maximum increase exceeding 45%. Moreover, the peak appears earlier as the parameter increases. Thus, extraction efficiency is one of the key processes governing displacement performance (Fig. 29(c)). The injection rate exhibits

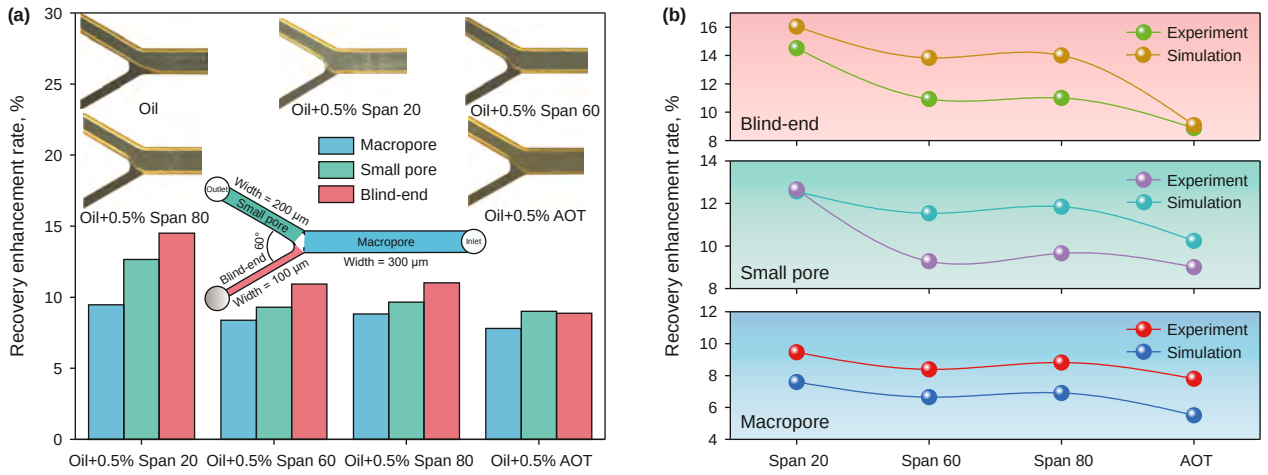


Fig. 28. Oil recovery under different pore and chemical agent conditions. **(a)** Experimental results statistics; **(b)** comparison of experimental and simulation results.

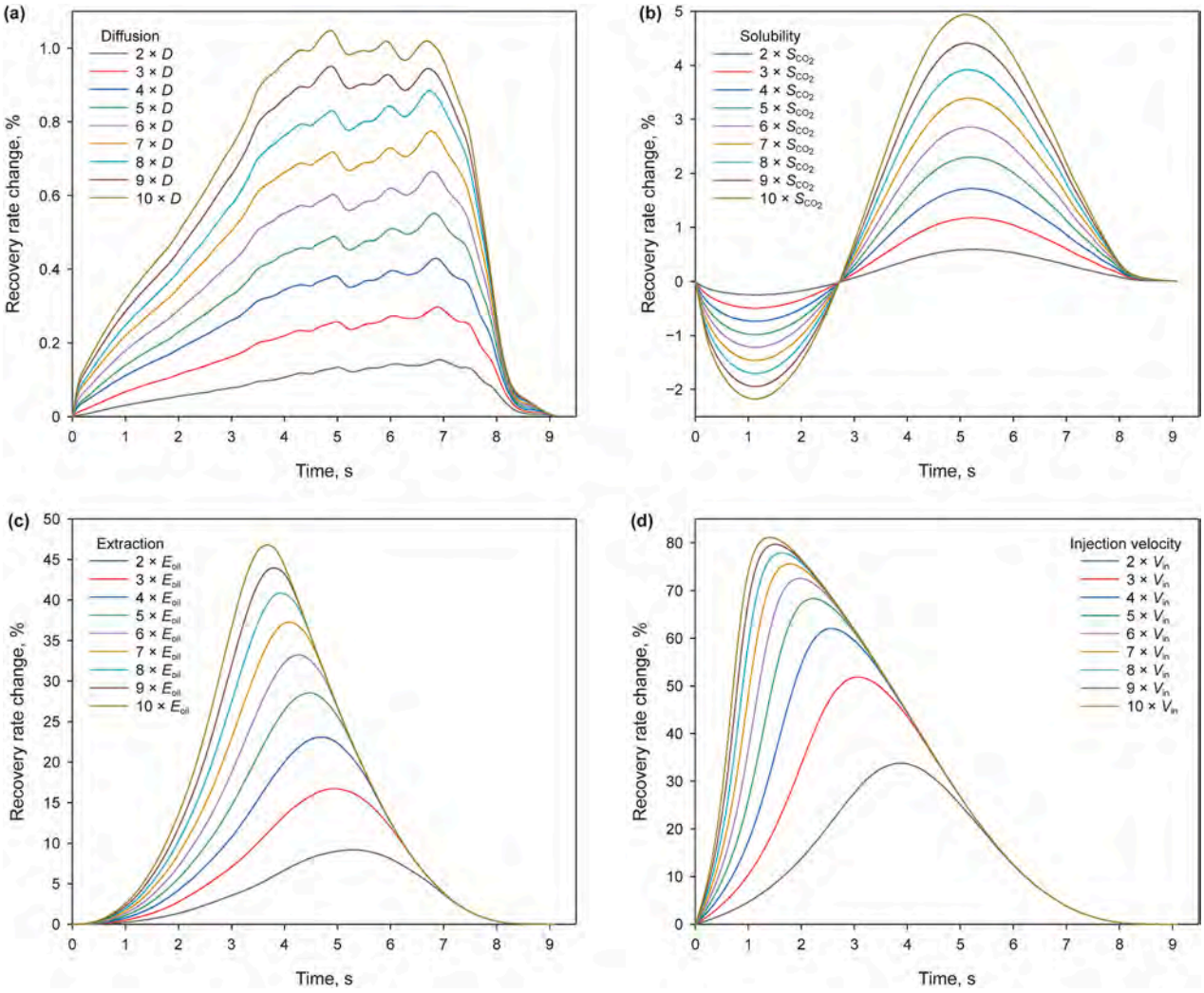


Fig. 29. Sensitivity of different parameters. **(a)** Diffusion coefficient; **(b)** solubility; **(c)** extraction efficiency; **(d)** injection velocity.

the strongest sensitivity among the four parameters, with the maximum improvement in recovery exceeding 80%. This indicates that the injection rate directly controls the displacement pressure gradient and sweep efficiency of CO_2 and is the dominant factor affecting oil recovery. However, the enhancement gradually diminishes when the injection rate is increased by about fourfold (Fig. 29(d)). A comprehensive comparison shows that the injection rate and extraction efficiency are the core controlling parameters affecting oil recovery, whereas the diffusion coefficient and CO_2 solubility have relatively smaller impacts.

3.4. Optimization of chemical agent concentration

The integrated molecular and pore-scale results indicate that 0.5% Span 20 gives the best enhanced oil recovery performance in the C8 system. Accordingly, this section focuses on optimizing the Span 20 concentration for the C8 system at the pore scale. The baseline simulation parameters are the same as those listed in Table 3.

3.4.1. Optimization schemes and parameters

Nine Span 20 concentration schemes were designed for the C8 system, ranging from 0.1% to 1.0% at intervals of 0.1%. The 0.5% case was already simulated in Section 3.3.1, so this part covers the remaining eight concentrations. The detailed experimental schemes and parameter settings are provided in Table 5.

Based on the molecular simulation results, the effects of varying Span 20 concentrations on CO_2 dissolution and extraction were incorporated into the CFD model via reaction source terms. Following the computational procedure described in Section 3.3.1, the influence of Span 20 concentration (0.1%–1.0%) on CO_2 dissolution and extraction was quantitatively analyzed. The correlation curves are provided in Appendix C (Figs. S1–S9 for dissolution and Figs. S10–S18 for extraction, corresponding to the schemes in Table 5). To accurately capture the concentration dependence, control functions for CO_2 dissolution and extraction at different Span 20 concentrations were established based on fitting results and are summarized in Table 6. These functions govern the dissolution and extraction processes of CO_2 in the C8 system across the tested concentrations.

Table 5
CFD optimization scheme.

Simulation scheme	Concentration of Span 20	Oil	Diffusion coefficient, $\times 10^{-8}$ m^2/s
①	0.1%	C8	0.6779
②	0.2%		0.5712
③	0.3%		0.6068
④	0.4%		0.5598
⑤	0.6%		0.6337
⑥	0.7%		0.5579
⑦	0.8%		0.5960
⑧	0.9%		0.5996
⑨	1.0%		0.5520

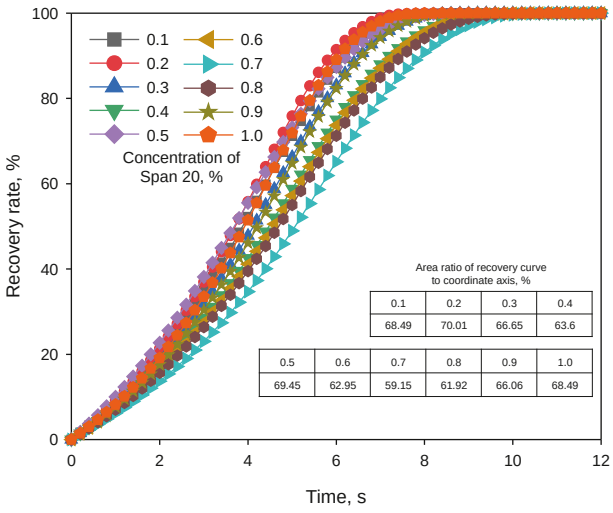


Fig. 30. Oil recovery under different Span 20 concentration conditions.

3.4.2. Optimization results

Based on the molecular simulation results and the schemes described above, nine simulation cases were conducted, and the oil recovery rates were statistically analyzed (Fig. 30). Displacement efficiency was quantified as the ratio of the area under the recovery curves to the total area of the coordinate plane. The results show that displacement efficiency fluctuates with Span 20 concentration. Specifically, as the concentration increased from 0.1% to 0.2%, efficiency rose by 1.52%; from 0.2% to 0.4%, it dropped by 6.41%; from 0.4% to 0.5%, it increased by 5.85%; from 0.5% to 0.7%, it decreased by 10.32%; and from 0.7% to 1.0%, it rose again by 9.36%. The peak efficiency occurred at 0.2% Span 20, while the minimum appeared at 0.7%, representing a difference of 10.88%. This non-monotonic behavior arises from the concentration-dependent regulation of CO_2 dissolution, extraction, and diffusion, combined with differential effects on oil recovery in macropore, small pore, and blind-end. A comprehensive analysis identifies 0.2% Span 20 as the optimal concentration for maximizing oil recovery through a synergistic mechanism.

3.4.3. Adsorption loss of chemicals

In the multiscale simulation framework established in this study, the selected optimal chemical agent exhibits good

Table 6
Solubility and extraction control functions at different concentrations of Span 20.

Concentration of Span 20, %	Solubility control function	R^2	Extraction control function	R^2
0.1	$y = 0.1354\ln(t) + 4.1044$	93.76%	$y = 0.2117\ln(t) + 5.6627$	94.84%
0.2	$y = 0.1498\ln(t) + 4.2976$	90.53%	$y = 0.2901\ln(t) + 7.2563$	87.87%
0.3	$y = 0.1133\ln(t) + 3.4670$	84.95%	$y = 0.2040\ln(t) + 5.3974$	87.66%
0.4	$y = 0.0980\ln(t) + 3.2482$	95.95%	$y = 0.1068\ln(t) + 3.5123$	91.00%
0.6	$y = 0.0791\ln(t) + 2.7533$	83.39%	$y = 0.1116\ln(t) + 3.5954$	86.51%
0.7	$y = 0.0410\ln(t) + 1.9446$	86.09%	$y = 0.0911\ln(t) + 3.0901$	88.71%
0.8	$y = 0.0691\ln(t) + 2.5980$	90.10%	$y = 0.1088\ln(t) + 3.2482$	85.02%
0.9	$y = 0.0993\ln(t) + 3.1813$	91.24%	$y = 0.2360\ln(t) + 5.9743$	88.33%
1	$y = 0.1106\ln(t) + 3.4475$	92.84%	$y = 0.3239\ln(t) + 7.9352$	87.24%

regulation performance and displacement adaptability under specific conditions. However, whether a chemical agent that performs well in an ideal environment can be effectively applied in actual oilfield development is subject to multiple coupled factors, including reservoir physicochemical interactions, geological characteristics, production techniques, and economic viability (Bhadani et al., 2016). In real reservoir environments, adsorption of chemical agents is the primary cause of effective concentration loss, and the actual conditions differ considerably from ideal ones. Moreover, complex geological environments such as high salinity, high clay content, and alkaline reservoirs can further exacerbate chemical loss (Saxena et al., 2019; Liu et al., 2020). Previous studies have confirmed that reservoirs with high clay content have a strong adsorption and retention effect on chemical agents; the concentration of the agent decays rapidly during transport along the seepage pathways between injection and production wells, with a loss rate of approximately 97% over a transport distance of only 20 m (Wang et al., 2024d). In conventional field applications, the injection concentration of chemical agents is usually controlled within 0.2%–0.5%, of which adsorption loss accounts for 30%–50%. When the adsorption loss rate exceeds 50%, the economic benefits of block development decline sharply (Ahmed et al., 2022; Li and Lv, 2026). Relevant data indicate that if the adsorption capacity of the reservoir rock for the chemical agent remains at 8–10 mg/g, the consumption of the agent in a single development block will reach 25–30 t, greatly increasing development costs and ultimately rendering the chemical agent economically unviable for reservoirs with high clay content and strong adsorption characteristics (Li and Lv, 2026). The adsorption of chemical agents is commonly evaluated using a Langmuir-type function (Muherei and Junin, 2009; Yusuf et al., 2021).

$$\Gamma = \frac{\Gamma_{\max} \times K_L \times C}{1 + K_L \times C} \tag{19}$$

The adsorption concentration per unit pore volume is given by:

$$C_{ads} = \frac{(1-\phi) \times \mathrm{Den}_{rock} \times \Gamma}{\phi} \tag{20}$$

The actual injection concentration is:

$$C_{act} = C_{eff} + C_{ads} \tag{21}$$

where Γ is the equilibrium adsorption capacity, mg/g; Γ_{max} is the maximum adsorption capacity, mg/g; K_L is the Langmuir adsorption constant, L/mg; C is the equilibrium concentration, mg/L; ϕ is the porosity, dimensionless; Den_{rock} is the rock density, g/cm^3; C_{ads} is the adsorption concentration per unit pore volume, mg/cm^3; C_{eff} is the effective concentration, mg/cm^3; C_{act} is the actual injection

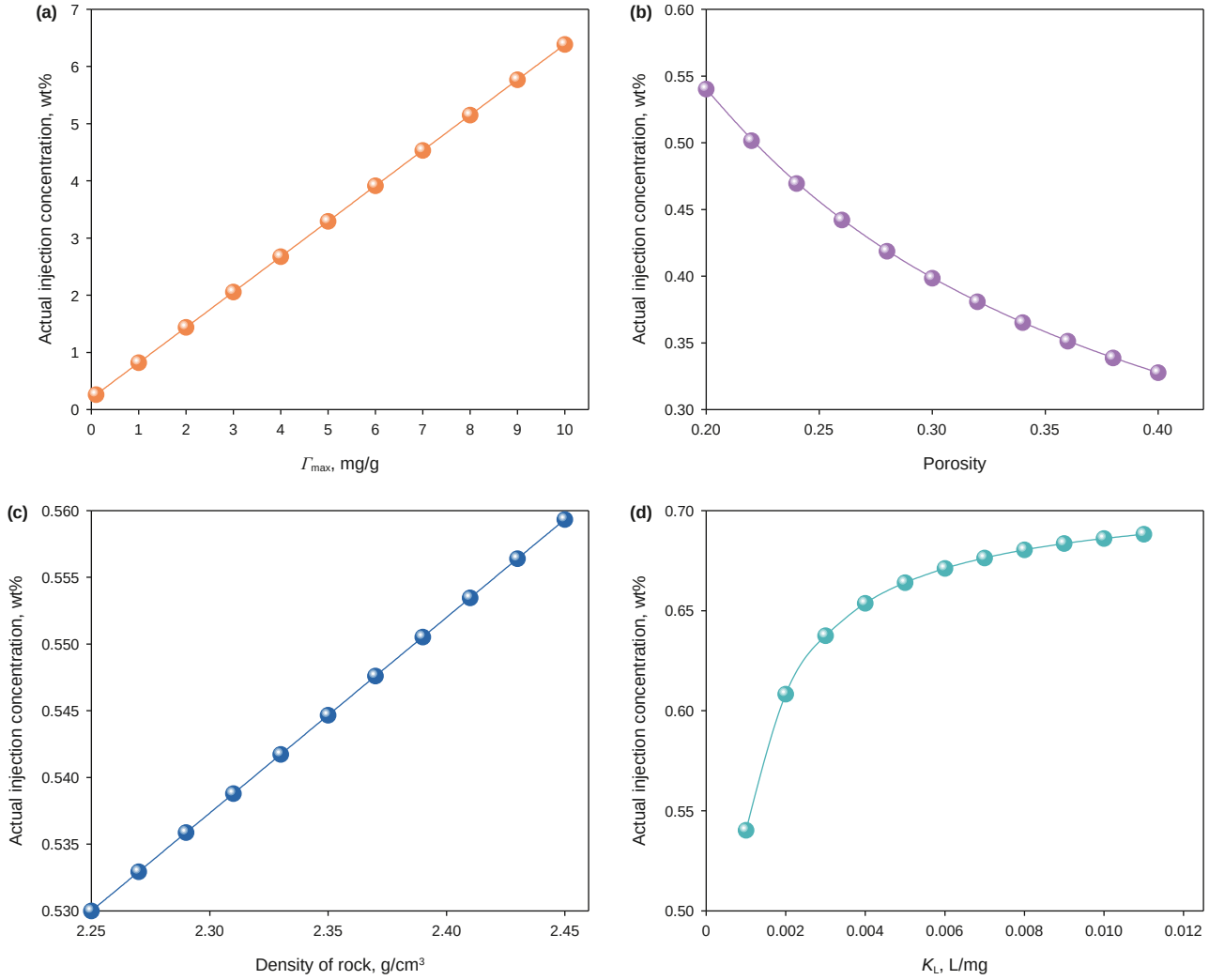


Fig. 31. Effects of different influencing factors on the actual injection concentration. **(a)** Maximum adsorption capacity (Γ_{max}); **(b)** porosity; **(c)** density of rock; **(d)** Langmuir adsorption constant (K_L).

concentration, mg/cm^3. For non-ionic surfactants in sandstone, the maximum adsorption capacity is approximately 0.55 mg/g (Muherei and Junin, 2009). The Langmuir adsorption constant is taken as 0.001–0.01 L/mg (Muherei and Junin, 2009). In this study, the equilibrium and effective concentrations of Span 20 are taken as the optimal concentration of 2000 mg/L (0.2 wt%). The porosity is set to 0.2, and the rock density is 2.32 g/cm^3.

With the above parameters fixed, the calculated actual injection concentration ranges from 0.54% to 0.68%. This indicates that to achieve the optimal effective chemical concentration (0.2%) in the formation, the actual injection concentration needs to be significantly higher than the theoretical value under ideal simulation conditions, with adsorption loss being the primary cause of this deviation. To systematically investigate the influence of various parameters on the actual injection concentration, a sensitivity analysis was conducted using the maximum adsorption capacity, porosity, rock density, and Langmuir adsorption constant as key variables (Fig. 31).

The results show that the maximum adsorption capacity is the dominant factor affecting the actual injection concentration. When the maximum adsorption capacity increases from 0.1 mg/g to 10 mg/g, the actual injection concentration rises sharply from 0.26% to 6.39% (Fig. 31(a)). This means that the stronger the adsorption capacity of the rock for the chemical agent, the higher the injection concentration required to compensate for adsorption loss. In practice, for reservoirs with strong adsorption characteristics (e.g., high clay mineral content), the injection concentration must be substantially increased or other measures taken; otherwise, the target effective concentration is difficult to achieve. Porosity is negatively correlated with the actual injection concentration. When porosity increases from 0.2 to 0.4, the actual injection concentration decreases from 0.54% to 0.33% (Fig. 31(b)). A higher porosity implies a reduction in the relative adsorption area of the rock skeleton and a larger volume fraction occupied by fluids, thereby reducing the additional injection needed to compensate for adsorption loss. This suggests that chemical flooding has certain advantages in high-porosity reservoirs. Rock density has a relatively weak, slightly positive correlation with the actual injection concentration. When rock density increases from 2.25 g/cm^3 to 2.42 g/cm^3, the actual injection concentration only rises slightly from 0.53% to 0.56% (Fig. 31(c)). Although a higher density increases the rock mass per unit volume and thereby the total number of available adsorption sites, the variation range of rock density in actual reservoirs is usually narrow, making this a secondary factor. The Langmuir adsorption constant is positively correlated with the actual injection concentration. When the Langmuir adsorption constant increases from 0.001 L/mg to 0.011 L/mg, the actual injection concentration rises from 0.54% to 0.69% (Fig. 31(d)). The Langmuir adsorption constant reflects the affinity strength between the chemical agent and the rock surface. A larger value indicates that the chemical agent is more easily adsorbed on the rock surface, requiring a higher injection concentration to overcome the adsorption effect. Notably, when the Langmuir adsorption constant is small, the actual injection concentration shows a greater increase, indicating that adsorption has not yet reached a competitive saturation state.

Combining the above sensitivity analysis, the influence of the various parameters on the actual injection concentration ranks as: maximum adsorption capacity $\gg$ Langmuir adsorption constant > porosity > rock density. Among these, the maximum adsorption capacity is the decisive factor, and a change in its order of magnitude can directly affect the economic feasibility of chemical flooding. This implies that in the design of chemical flooding schemes, priority should be given to accurately determining the maximum adsorption capacity through core adsorption experiments. Furthermore, there is a large gap between the actual injection concentration and the optimal effective concentration, indicating that most of the injected chemical agent will be lost to rock adsorption. Therefore, in strongly adsorbing reservoirs, simply increasing the injection concentration is not the optimal strategy. Instead, combined approaches such as nanofluid modification or the co-injection of adsorption inhibitors should be adopted to reduce the adsorption capacity of the rock at the source, thereby balancing technical effectiveness and economic viability.

4. Conclusions

This study used multiscale simulations, including theoretical calculations, molecular dynamics, and computational fluid dynamics, to investigate the microscopic mechanisms of chemical-assisted CO_2 flooding in deep reservoirs. A pore-scale flooding model that accounts for multiple chemical effects was developed, and a cross-scale chemical-optimization strategy was established. The principal conclusions are as follows.

(1) A multiscale coupling model was developed to bridge molecular-scale interactions and pore-scale flow, providing a quantitative method for characterizing the regulatory effects of chemicals on the CO_2-oil system through parameters such as interaction energy and diffusion coefficients.
(2) The chemical regulation mechanisms governing CO_2 dissolution, extraction, and diffusion in oil were clarified. Span 20 showed concentration-dependent performance: at 0.1%, CO_2 solubility in C8 increased by 20.64% and the diffusion coefficient increased by 12.38%; at 0.5%, extraction efficiency increased by 44.60%. Pore-structure complexity under high-temperature/high-pressure conditions also modulated diffusion-concentration relationships.
(3) The mechanistic role of chemical agents in CO_2 flooding was identified. CO_2-oil interaction intensity decreased with increasing hydrocarbon chain length. Chemicals enhanced recovery by reducing oil-rock interaction energy, with the optimum effect observed at 0.2% Span 20, thereby facilitating oil displacement from pore walls. The performance ranking was Span 20 > Span 60/Span 80 > AOT.
(4) A predictive pore-scale model for chemical-assisted CO_2 flooding was established. Recovery efficiency consistently decreased as carbon number increased across all pore types. Span-series agents markedly improved recovery from small and blind-end pores, whereas AOT mainly enhanced recovery from small pores.
(5) A cross-scale method for optimizing chemical concentration was proposed. For C8, 0.2% Span 20 was identified as the optimal concentration for CO_2 flooding because it maximized the synergistic effects of dissolution, extraction, and diffusion. Based on the sensitivity analysis of rock adsorption, the practical injection concentration should be maintained between 0.54% and 0.68% to ensure engineering effectiveness in deep reservoirs.

5. Limitations and future perspectives

Although the multiscale framework established in this study elucidates the mechanisms of chemical-assisted CO_2 flooding, several limitations should be acknowledged. First, the molecular and pore-scale simulations were conducted under specific deep-

reservoir conditions and did not consider formation-water salinity, which is a key factor affecting surfactant performance. High salinity may cause surfactant precipitation, alter the critical micelle concentration, and change rock wettability, thereby shifting the optimal chemical type and concentration. Future work should incorporate electrolyte effects and geochemical reactions to evaluate chemical stability under more realistic reservoir conditions.

Second, the chemical concentration optimized through multi-scale simulation was mainly determined from its synergistic advantages in dissolution, extraction, diffusion, and microscopic residual-oil mobilization. In field applications, however, economic feasibility, surfactant adsorption loss, and potential formation damage must also be considered. Field injection design should balance surfactant cost, injection scale, and incremental oil production, with profitability further influenced by oil price, CO_2 source cost, and enhanced-recovery degree. Because chemical adsorption onto rock is controlled by mineral composition, salinity, and temperature, future work should quantify adsorption through static adsorption experiments and mitigate it using anti-adsorption additives.

Third, improving microscopic seepage conditions at the pore scale can help expand macroscopic sweep volume and enhance oil recovery. However, upscaling microscopic mechanisms to the reservoir scale remains challenging because of pore connectivity, rock wettability, injection parameters, and pressure gradients. The pore-scale results and microscopic mechanisms reported here provide a theoretical basis and parameter support for subsequent reservoir-scale simulations and field injection design, thereby improving the engineering applicability of chemical-assisted CO_2 flooding.

CRediT authorship contribution statement

Quan-Ling Qin: Writing – original draft, Software, Investigation, Conceptualization. **Jian Hou:** Supervision, Investigation, Funding acquisition, Formal analysis, Conceptualization. **Kang Zhou:** Writing – review & editing, Investigation, Formal analysis. **Jia-Rui Zhang:** Methodology. **Hao-Yu Zheng:** Methodology. **Yong-Sheng Liu:** Visualization, Methodology. **Bei Wei:** Visualization, Formal analysis. **Teng Lu:** Software, Methodology. **Yong-Ge Liu:** Conceptualization. **Wei-Bing Tian:** Validation, Software. **Qing-Jun Du:** Visualization, Methodology.

Declaration of competing interest

The authors declare that they have no known competing financial interests or personal relationships that could have appeared to influence the work reported in this paper.

Acknowledgments

The writers greatly appreciate the financial support of the Taishan Scholars Program, the Shandong Provincial Natural Science Foundation (Grant No. ZR2025MS747), and the Important National Science and Technology Specific Projects of China (Grant No. 2025ZD1406101).

Supplementary data

Supplementary data to this article can be found online at https://doi.org/10.1016/j.petsci.2026.06.050.

References

Afshari, S., Hejazi, S.H., Kantzas, A., 2018. Longitudinal dispersion in heterogeneous layered porous media during stable and unstable pore-scale miscible displacements. Adv. Water Resour. 119, 125–141. https://doi.org/10.1016/j.advwatres.2018.06.005.

Ahmed, K.R., Kalam, S., Norrman, K., et al., 2022. Ionic liquids as clay swelling inhibitors: adsorption study. Energy Fuels 36 (7), 3596–3605. https://doi.org/10.1021/acs.energyfuels.2c00088.

Alharthy, N., Teklu, T., Kazemi, H., et al., 2017. Enhanced oil recovery in liquid-rich shale reservoirs: Laboratory to field. SPE Reservoir Eval. Eng 21 (1), 137–159. https://doi.org/10.2118/175034-PA.

Aziz, R., Niasar, V., Erfani, H., et al., 2020. Impact of pore morphology on two-phase flow dynamics under wettability alteration. Fuel 268, 117315. https://doi.org/10.1016/j.fuel.2020.117315.

Bhadani, A., Misono, T., Singh, S., et al., 2016. Structural diversity, physicochemical properties and application of imidazolium surfactants: Recent advances. Adv. Colloid Interface Sci. 231, 36–58. https://doi.org/10.1016/j.cis.2016.03.005.

Chen, H., Liu, X.L., Zhang, C., et al., 2022. Effects of miscible degree and pore scale on seepage characteristics of unconventional reservoirs fluids due to supercritical CO_2 injection. Energy 239, 122287. https://doi.org/10.1016/j.energy.2021.122287.

Chowdhury, S., Rakesh, M., Medhi, S., et al., 2022. Pore-scale flow simulation of supercritical CO_2 and oil flow for simultaneous CO_2 geo-sequestration and enhanced oil recovery. Environ. Sci. Pollut. Res. 29, 76003–76025. https://doi.org/10.1007/s11356-022-21217-7.

Cui, W.G., Liang, Y.F., Masuda, Y., et al., 2023. Estimation of the minimum miscibility pressure for CO_2-crude-oil systems by molecular dynamics simulation. Pet Res 8, 1–10. https://doi.org/10.1016/j.ptlrs.2022.08.001.

Feng, Q.H., Xing, X.D., Wang, S., et al., 2024. CO_2 diffusion in shale oil based on molecular simulation and pore network model. Fuel 359, 130332. https://doi.org/10.1016/j.fuel.2023.130332.

Gao, H.X., Zhang, B., Fan, L.L., et al., 2019. Study on diffusivity of CO_2 in oil-saturated porous media under high pressure and temperature. Energy Fuels 33 (11), 11364–11372. https://doi.org/10.1021/acs.energyfuels.9b01947.

Guo, Y.H., Liu, F., Qiu, J.J., et al., 2022. Microscopic transport and phase behaviors of CO_2 injection in heterogeneous formations using microfluidics. Energy 256, 124524. https://doi.org/10.1016/j.energy.2022.124524.

Guénolé, J., Nöhring, W.G., Vaid, A., et al., 2020. Assessment and optimization of the fast inertial relaxation engine (fire) for energy minimization in atomistic simulations and its implementation in lammps. Comput. Mater. Sci. 175, 109584. https://doi.org/10.1016/j.commatsci.2020.109584.

Heidaryan, E., Hatami, T., Rahimi, M., et al., 2011. Viscosity of pure carbon dioxide at supercritical region: Measurement and correlation approach. J. Supercrit. Fluids 56 (2), 144–151. https://doi.org/10.1016/j.supflu.2010.12.006.

Hu, Y.S., Wang, H., Guo, P., et al., 2025. Molecular insights into CO_2-EOR/CCUS: Nanoconfinement effects on multi-component diffusion and miscibility in shale reservoirs. Fuel 395, 135238. https://doi.org/10.1016/j.fuel.2025.135238.

Huang, T., Cheng, L.S., Cao, R.Y., et al., 2024. Molecular simulation of the dynamic distribution of complex oil components in shale nanopores during CO_2-EOR. Chem. Eng. J. 479, 147743. https://doi.org/10.1016/j.cej.2023.147743.

Jiang, Y., Qiu, J.J., Shi, J.W., et al., 2024. Rapid determination of volumetric mass transfer coefficients for CO_2-crude oil systems using microfluidics. Ind. Eng. Chem. Res. 63 (25), 11196–11206. https://doi.org/10.1021/acs.iecr.4c00324.

Jin, Z.H., Firoozabadi, A., 2016. Phase behavior and flow in shale nanopores from molecular simulations. Fluid Phase Equilib. 430, 156–168. https://doi.org/10.1016/j.fluid.2016.09.011.

Kumar, N., Augusto, S.M., Ojha, K., et al., 2022. Fundamental aspects, mechanisms and emerging possibilities of CO_2 miscible flooding in enhanced oil recovery: A review. Fuel 330, 125633. https://doi.org/10.1016/j.fuel.2022.125633.

Lei, Z.D., Liu, Y.H., Wang, R., et al., 2022. A microfluidic experiment on CO_2 injection for enhanced oil recovery in a shale oil reservoir with high temperature and pressure. Energies 15 (24), 9461. https://doi.org/10.3390/en15249461.

Li, S.Y., Li, Z.M., Dong, Q.W., 2016. Diffusion coefficients of supercritical CO_2 in oil-saturated cores under low permeability reservoir conditions. J. CO2 Util. 14, 47–60. https://doi.org/10.1016/j.jcou.2016.02.002.

Li, S.Y., Qiao, C.Y., Zhang, C., et al., 2018. Determination of diffusion coefficients of supercritical CO_2 under tight oil reservoir conditions with pressure-decay method. J. CO2 Util. 24, 430–443. https://doi.org/10.1016/j.jcou.2018.02.002.

Li, X.F., Wang, P., Wang, S., et al., 2021. Dynamics and miscible behaviors of hydrocarbon gas and crude oil in nanoslits: Effects of light gas type and crude oil components. Chem. Eng. J. 405, 127012. https://doi.org/10.1016/j.cej.2020.127012.

Li, S.Y., Wang, L., Su, L.N., et al., 2022a. Carbon dioxide diffusions in methane-dissolved pore fluids: Implications for geological carbon storage and utilization in tight formations. Chem. Eng. J. 429, 132147. https://doi.org/10.1016/j.cej.2021.132147.

Li, G.X., Zheng, F.J., Huang, Q.F., et al., 2022b. Molecular insight into pyrolysis processes via reactive force field molecular dynamics: A state-of-the-art review. J. Anal. Appl. Pyrolysis 166, 105620. https://doi.org/10.1016/j.jaap.2022.105620.

Li, L., Zhou, X.M., Wang, R.J., et al., 2023a. Microscopic experiment study on mechanisms of oil-gas interaction and CO_2-surfactant flooding with different

temperatures and pressures. J. CO2 Util. 69, 102389. https://doi.org/10.1016/j.jcou.2022.102389.
Li, Z.F., Liu, J.H., Su, Y.L., et al., 2023b. Influences of diffusion and advection on dynamic oil-CO_2 mixing during CO_2 EOR and storage process: Experimental study and numerical modeling at pore-scales. Energy 267, 126567. https://doi.org/10.1016/j.energy.2022.126567.
Li, S., Liang, Y.F., Jiang, F., et al., 2024. Multiscale simulation of water/oil displacement with dissolved CO_2: Implications for geological carbon storage and CO_2-enhanced oil recovery. Chem. Eng. J. 499, 155936. https://doi.org/10.1016/j.cej.2024.155936.
Li, M.Y., Lv, N.B., 2026. Surfactant-enhanced oil recovery from an interfacial perspective: Multiscale mechanisms, adsorption loss, and performance boundaries under realistic reservoir conditions. J. Dispersion Sci. Technol. 1–17. https://doi.org/10.1080/01932691.2026.2635438.
Liu, Y., Teng, Y., Lu, G.H., et al., 2016. Experimental study on CO_2 diffusion in bulk n-decane and n-decane saturated porous media using micro-CT. Fluid Phase Equilib. 417, 212–219. https://doi.org/10.1016/j.fluid.2016.02.034.
Liu, Z.L., Hedayati, P., Sudhölter, E.J.R., et al., 2020. Adsorption behavior of anionic surfactants to silica surfaces in the presence of calcium ion and polystyrene sulfonate. Colloids Surf., A 602, 125074. https://doi.org/10.1016/j.colsurfa.2020.125074.
Liu, Y.L., Rui, Z.H., Yang, T., et al., 2022a. Using propanol as an additive to CO_2 for improving CO_2 utilization and storage in oil reservoirs. Appl. Energy 311, 118640. https://doi.org/10.1016/j.apenergy.2022.118640.
Liu, Z.W., Cui, X.C., Su, X., et al., 2022b. Experimental study on the diffusion characteristics of the miscible $ScCO_2$/oil system based on the droplet interface shrinkage behavior. Colloids Surf., A 637, 128234. https://doi.org/10.1016/j.colsurfa.2021.128234.
Liu, F.N., Wang, X.Z., Yang, H., et al., 2024. Miscibility characteristics of CO_2-oil in tight sandstone reservoirs: Insights from molecular dynamics simulations. ACS Omega 9 (13), 15663–15676. https://doi.org/10.1021/acsomega.4c00541.
Liu, X.L., Chen, H., Cheng, W.M., et al., 2025a. Occurrence states and transport behavior of crude oil in different permeability oil reservoirs during depletion development. Geoenergy Sci. Eng. 252, 213944. https://doi.org/10.1016/j.geoen.2025.213944.
Liu, X.L., Chen, H., Li, Y., et al., 2025b. Oil production characteristics and CO_2 storage mechanisms of CO_2 flooding in ultra-low permeability sandstone oil reservoirs. Petrol. Explor. Dev. 52 (1), 196–207. https://doi.org/10.1016/S1876-3804(25)60014-0.
Lu, N., Dong, X.H., Chen, Z.X., et al., 2022. Effect of solvent on the adsorption behavior of asphaltene on silica surface: A molecular dynamic simulation study. J. Pet. Sci. Eng. 212, 110212. https://doi.org/10.1016/j.petrol.2022.110212.
Lu, T., Li, Z.M., Gu, Z.H., et al., 2023. Stability and enhanced oil recovery performance of CO_2 in water emulsion: Experimental and molecular dynamic simulation study. Chem. Eng. J. 464, 142636. https://doi.org/10.1016/j.cej.2023.142636.
Lu, T., Li, Z.M., Du, L.P., 2024a. Enhancing foam stability and addressing asphaltene deposition for improved oil recovery in CCUS applications using aerogel nanoparticles. Chem. Eng. J. 481, 148290. https://doi.org/10.1016/j.cej.2023.148290.
Lu, N., Dong, X.H., Liu, H.Q., et al., 2024b. Molecular insights into the synergistic mechanisms of hybrid CO_2-surfactant thermal systems at heavy oil-water interfaces. Energy 286, 129476. https://doi.org/10.1016/j.energy.2023.129476.
Luo, Y.C., Xiao, H.M., Liu, X.G., et al., 2023. Diffusion coefficient and the volume swelling of CO_2/light oil systems: Insights from dynamic volume analysis and molecular dynamics simulation. J. Mol. Liq. 382, 121943. https://doi.org/10.1016/j.molliq.2023.121943.
Lv, W., Dong, M.Z., Sarma, H., et al., 2023. Effects of CO_2-philic nonionic polyether surfactants on miscibility behaviors of CO_2-hydrocarbon systems: experimental and simulation approach. Chem. Eng. J. 464, 142701. https://doi.org/10.1016/j.cej.2023.142701.
Moniruzzaman, M., Kamiya, N., Goto, M., 2010. Ionic liquid based microemulsion with pharmaceutically accepted components: Formulation and potential applications. J. Colloid Interface Sci. 352 (1), 136–142. https://doi.org/10.1016/j.jcis.2010.08.035.
Muherei, M.A., Junin, R., 2009. Equilibrium adsorption isotherms of anionic, nonionic surfactants and their mixtures to shale and sandstone. Mod. Appl. Sci. 3 (2), 158–167. https://doi.org/10.5539/mas.v3n2p158.
Pan, X.X., Sun, L.H., Chen, F.Y., et al., 2024. Minimum miscibility pressure of the CO_2-hydrocarbon system based on nanofluidics. Energy Fuels 38 (12), 10904–10913. https://doi.org/10.1021/acs.energyfuels.4c01556.
Pedersen, K.S., Fredenslund, A., Christensen, P.L., et al., 1984. Viscosity of crude oils. Chem. Eng. Sci. 39 (6), 1011–1016. https://doi.org/10.1016/0009-2509(84)87009-8.
Peng, D.Y., Robinson, D.B., 1976. A new two-constant equation of state. Ind. Eng. Chem. Fundam. 15 (1), 59–64. https://doi.org/10.1021/i160057a011.
Ren, J.T., Xiao, W.L., Pu, W.F., et al., 2024. Characterization of CO_2 miscible/immiscible flooding in low-permeability sandstones using NMR and the VOF simulation method. Energy 297, 131211. https://doi.org/10.1016/j.energy.2024.131211.
Saxena, N., Kumar, A., Mandal, A., 2019. Adsorption analysis of natural anionic surfactant for enhanced oil recovery: the role of mineralogy, salinity, alkalinity and nanoparticles. J. Pet. Sci. Eng. 173, 1264–1283. https://doi.org/10.1016/j.petrol.2018.11.002.
Song, R., Tang, Y., Wang, Y., et al., 2022. Pore-scale numerical simulation of CO_2-oil two-phase flow: a multiple-parameter analysis based on phase-field method. Energies 16 (1), 82. https://doi.org/10.3390/en16010082.
Song, X.M., Wang, F., Ma, D.S., et al., 2023. Progress and prospect of carbon dioxide capture, utilization and storage in CNPC oilfields. Petrol. Explor. Dev. 50 (1), 229–244. https://doi.org/10.1016/S1876-3804(22)60383-5.
Song, G.L., Meng, Y.X., Zhang, C.L., et al., 2024. Comprehensive review of the determination and reduction of the minimum miscibility pressure during CO_2 flooding. ACS Omega 9 (13), 14747–14765. https://doi.org/10.1021/acsomega.4c00469.
Ssebadduka, R., Kono, H., Sasaki, K., et al., 2020. Measurements of CO_2 molecular diffusion coefficients in crude oils from swelling-time curve and estimation using viscosity from the stokes-einstein formula. J. Pet. Sci. Eng. 187, 106823. https://doi.org/10.1016/j.petrol.2019.106823.
Sun, H., 1998. COMPASS: An ab initio force-field optimized for condensed-phase applications overview with details on alkane and benzene compounds. J. Phys. Chem. B 102 (38), 7338–7364. https://doi.org/10.1021/jp980939v.
Sun, Q., Zhang, N., Zhu, P., et al., 2024. Confined fluid interfacial tension and minimum miscibility pressure prediction in shale nanopores. Fuel 364, 130949. https://doi.org/10.1016/j.fuel.2024.130949.
Türkmenoğlu, A., Önel, S., 2025. Chemical assisted reduction on minimum miscibility pressure of viscous crude oils. Fuel 379, 133006. https://doi.org/10.1016/j.fuel.2024.133006.
Upreti, S.R., Mehrotra, A.K., 2000. Experimental measurement of gas diffusivity in bitumen: results for carbon dioxide. Ind. Eng. Chem. Res. 39 (4), 1080–1087. https://doi.org/10.1021/ie990635a.
Vinogradova, O.I., 1995. Drainage of a thin liquid film confined between hydrophobic surfaces. Langmuir 11 (6), 2213–2220. https://doi.org/10.1021/la00006a059.
Wang, P., Li, X.F., Tao, Z.W., et al., 2021. The miscible behaviors and mechanism of CO_2/CH_4/C_3H_8/N_2 and crude oil in nanoslits: a molecular dynamics simulation study. Fuel 304, 121461. https://doi.org/10.1016/j.fuel.2021.121461.
Wang, H., Su, Y.L., Wang, W.D., et al., 2022. CO_2-oil diffusion, adsorption and miscible flow in nanoporous media from pore-scale perspectives. Chem. Eng. J. 450, 137957. https://doi.org/10.1016/j.cej.2022.137957.
Wang, Z.J., Zhu, J.Z., Li, S.Y., 2023. Novel strategy for reducing the minimum miscible pressure in a CO_2-oil system using nonionic surfactant: Insights from molecular dynamics simulations. Appl. Energy 352, 121966. https://doi.org/10.1016/j.apenergy.2023.121966.
Wang, Y.H., Lei, Z.D., Sun, L.H., et al., 2024a. Study on the minimum miscibility pressure and phase behavior of CO_2-shale oil in nanopores. Chem. Eng. J. 497, 154493. https://doi.org/10.1016/j.cej.2024.154493.
Wang, L., Zou, R., Yuan, Y.F., et al., 2024b. Dynamics of impure CO_2 and composite oil in mineral nanopores: Implications for shale oil recovery and gas storage performance. Chem. Eng. J. 500, 157421. https://doi.org/10.1016/j.cej.2024.157421.
Wang, J.Y., Tian, K., Li, Y., et al., 2024c. Diffusion coefficients of polycyclic aromatic hydrocarbons in supercritical carbon dioxide: A molecular dynamics simulation study. J. Mol. Liq. 409, 125457. https://doi.org/10.1016/j.molliq.2024.125457.
Wang, Y.Y., Qin, D.P., Jiang, S.D., 2024d. Adsorption behavior of different components of a polymer/surfactant composite control system along an injection-production channel in sand conglomerate reservoirs. ACS Omega 9 (39), 40665–40675. https://doi.org/10.1021/acsomega.4c04906.
Wang, S., Zhang, M.Q., Zhang, Y.L., et al., 2025. Mechanisms of CO_2 huff and puff enhanced oil recovery and storage within shale nanopores. Chem. Eng. J. 506, 160098. https://doi.org/10.1016/j.cej.2025.160098.
Xiang, Y., Hou, L., Du, M., et al., 2023. Research progress and development prospect of CCUS-EOR technologies in China. Pet Geol Recover Effic 30 (2), 1–17. https://doi.org/10.13673/j.cnki.cn37-1359/te.202112048 (in Chinese).
Xie, C.Y., Huang, J.W., Li, Y.P., et al., 2025. Interfacial property and minimum miscibility pressure of dimethyl ether-assisted CO_2 and bakken oil: A molecular dynamics study. SPE J. 30 (9), 5810–5822. https://doi.org/10.2118/228322-PA.
Xiong, C.M., Li, S.J., Ding, B., et al., 2021. Molecular insight into the oil displacement mechanism of gas flooding in deep oil reservoir. Chem. Phys. Lett. 783, 139044. https://doi.org/10.1016/j.cplett.2021.139044.
Xue, C.L., Ji, D.L., Wen, Y.T., et al., 2023. Promising combination of CO_2 enhanced oil recovery and CO_2 sequestration in calcite nanoslits: Insights from molecular dynamics simulations. J. Mol. Liq. 391, 123243. https://doi.org/10.1016/j.molliq.2023.123243.
Yan, Z.C., Li, X.F., Zhu, X., et al., 2023. MD-CFD simulation on the miscible displacement process of hydrocarbon gas flooding under deep reservoir conditions. Energy 263, 125730. https://doi.org/10.1016/j.energy.2022.125730.
Yang, Y., 2020. Research and application of CO_2 flooding technology in extra-low permeability reservoirs of shengli oilfield. Pet Geol Recover Effic 27 (1), 11–19. https://doi.org/10.13673/j.cnki.cn37-1359/te.2020.01.002 (in Chinese).
Yang, X.M., Zhang, M.L., Gao, Y., et al., 2021. Molecular dynamics study on viscosities of sub/supercritical n-decane, n-undecane and n-dodecane. J. Mol. Liq. 335, 116180. https://doi.org/10.1016/j.molliq.2021.116180.
Yang, Y., Zhang, S.M., Cao, X.P., et al., 2024. CO_2 high-pressure miscible flooding and storage technology and its application in shengli oilfield, China. Petrol. Explor. Dev. 51 (5), 1247–1260. https://doi.org/10.1016/S1876-3804(25)60538-6.
Yu, T., Li, Q., Tan, Y.S., et al., 2023. Characterization of the effects of wettability and pore pressure on the interfacial behavior of CO_2 interacting with oil-water

two-phase on pore walls. Geoenergy Sci. Eng. 231, 212329. https://doi.org/10.1016/j.geoen.2023.212329.
Yuan, L., Zhang, Y., Liu, S.Z., et al., 2023. Molecular dynamics simulation of CO_2-oil miscible fluid distribution and flow within nanopores. J. Mol. Liq. 380, 121769. https://doi.org/10.1016/j.molliq.2023.121769.
Yusuf, M., Wathon, M.H., Thanasaksukthawee, V., et al., 2021. Adsorption of saponin natural surfactant on carbonate rock and comparison to synthetic surfactants: An enhanced oil recovery prospective. Energy Fuels 35 (14), 11193–11202. https://doi.org/10.1021/acs.energyfuels.1c00721.
Zhang, C., Li, Z.M., Li, S.Y., et al., 2018. Enhancing sodium bis(2-ethylhexyl) sulfosuccinate injectivity for CO_2 foam formation in low-permeability cores: dissolving in CO_2 with ethanol. Energy Fuels 32 (5), 5846–5856. https://doi.org/10.1021/acs.energyfuels.8b00741.
Zhang, M.S., Zhan, S.Y., Jin, Z.H., 2020a. Recovery mechanisms of hydrocarbon mixtures in organic and inorganic nanopores during pressure drawdown and CO_2 injection from molecular perspectives. Chem. Eng. J. 382, 122808. https://doi.org/10.1016/j.cej.2019.122808.
Zhang, C., Xi, L.H., Wu, P.K., et al., 2020b. A novel system for reducing CO_2-crude oil minimum miscibility pressure with CO_2-soluble surfactants. Fuel 281, 118690. https://doi.org/10.1016/j.fuel.2020.118690.
Zhang, X., Li, L., Da, Q.A., et al., 2022a. Microfluidic investigation on multiphase interaction and flow behavior of immiscible/miscible gases in deep heterogeneous reservoir. J. Environ. Chem. Eng. 10 (6), 109036. https://doi.org/10.1016/j.jece.2022.109036.
Zhang, X., Su, Y.L., Li, L., et al., 2022b. Microscopic remaining oil initiation mechanism and formation damage of CO_2 injection after waterflooding in deep reservoirs. Energy 248, 123649. https://doi.org/10.1016/j.energy.2022.123649.
Zhang, X., Li, L., Su, Y.L., et al., 2023. Microfluidic investigation on asphaltene interfaces attempts to carbon sequestration and leakage: Oil-CO_2 phase interaction characteristics at ultrahigh temperature and pressure. Appl. Energy 348, 121518. https://doi.org/10.1016/j.apenergy.2023.121518.
Zhang, D., Li, L., Wang, H., et al., 2024. Study on the mechanism of CO_2 huff-n-puff enhanced oil recovery and storage in shale porous media considering heterogeneous structure. Phys. Fluids 36 (7), 072005. https://doi.org/10.1063/5.0210933.
Zheng, S.X., Li, H.A., Sun, H.J., et al., 2016. Determination of diffusion coefficient for alkane solvent-CO_2 mixtures in heavy oil with consideration of swelling effect. Ind. Eng. Chem. Res. 55 (6), 1533–1549. https://doi.org/10.1021/acs.iecr.5b03929.
Zhou, X., Jiang, Q., Yuan, Q.W., et al., 2020. Determining CO_2 diffusion coefficient in heavy oil in bulk phase and in porous media using experimental and mathematical modeling methods. Fuel 263, 116205. https://doi.org/10.1016/j.fuel.2019.116205.
Zhu, G.P., Yao, J., Li, A.F., et al., 2017. Pore-scale investigation of carbon dioxide-enhanced oil recovery. Energy Fuels 31 (5), 5324–5332. https://doi.org/10.1021/acs.energyfuels.7b00058.
Zhu, Q.Y., Wu, K.L., Guo, S.Q., et al., 2024. Pore-scale investigation of CO_2-oil miscible flooding in tight reservoir. Appl. Energy 368, 123439. https://doi.org/10.1016/j.apenergy.2024.123439.